

## Oscillations of a Water Droplet onto a Horizontally Vibrating Substrate

King L. Ng\*,<sup>1</sup> Luís H. Carnevale,<sup>1</sup> Michał Klamka,<sup>2</sup> Piotr Deuar,<sup>1</sup> Tomasz Bobinski,<sup>2</sup>  
and Panagiotis E. Theodorakis<sup>1</sup>

<sup>1</sup>*Institute of Physics, Polish Academy of Sciences, Al. Lotników 32/46, 02-668 Warsaw, Poland*

<sup>2</sup>*Institute of Aeronautics and Applied Mechanics, Warsaw University of Technology, Nowowiejska 24, 02-665 Warsaw, Poland*

(\*Electronic mail: klng@ifpan.edu.pl)

(Dated: 20 December 2024)

Deformed droplets are ubiquitous in various industrial applications, such as inkjet printing, lab-on-a-chip devices, and spray cooling, and can fundamentally affect the involved applications both favorably and unfavorably. Here, we employ many-body dissipative particle dynamics to investigate the oscillations of water droplets on a harmonically and horizontally vibrating, solid substrate. Three distinct scenarios of oscillations as a response to the substrate vibrations have been identified. The first scenario reflects a common situation where the droplet can follow the substrate vibrations. In the other two scenarios, favored in the case of hydrophilic substrates, droplet oscillations generate high shear rates that ultimately lead to droplet breakup. Leveraging our simulation model, the properties of the droplet and the mechanisms related to the oscillations are analyzed with a molecular-level resolution, while results are also put in the perspective of experiment. Our study suggests that the three scenarios can be distinguished by the contact-surface velocity of the oscillating droplet, with threshold velocities influenced by the substrate's wettability. Moreover, the mean magnitude of the particle velocity at the contact surface plays a key role in determining the three oscillation phases, suggesting that the capillary number of the oscillating droplet governs the phase behavior. Thus, our approach aims to optimize droplet oscillations and deformations on solid substrates, which have direct implications for technological applications.

## I. INTRODUCTION

Many industrial applications involve deforming droplets on a solid substrate, for example, in lab-on-a-chip applications,<sup>1</sup> inkjet printing,<sup>2</sup> spray cooling,<sup>3</sup> and combustion,<sup>4</sup> just to mention a few. In such applications, vibrations can impact the performance at the elementary level.<sup>5</sup> For example, on the one hand, droplet shape oscillations caused by vibrations can lead to undesirable droplet breakup<sup>6</sup>. On the other hand, understanding the role of oscillations at the droplet level can be exploited to enhance the mixing within the droplet in microfluidics applications<sup>7,8</sup> or in an oscillating droplet tribometer.<sup>9</sup>

The oscillations of drops, in general, have been investigated in the case of free droplets, namely those falling or floating freely in their surroundings, as well as constrained drops, for example, a drop constrained by a rod that is forced to oscillate in a fluid of similar density to remove the effects of gravity, thus enabling the study of pure surface tension restored oscillations.<sup>10</sup> Moreover, oscillations can be categorized as axisymmetric or non-axisymmetric surface oscillations, that is, surface oscillations caused by vertical or horizontal vibrations, respectively.<sup>11</sup> While the oscillation of constrained drops has only been considered over the last decades,<sup>10</sup> that of free drops is a much more long-standing topic of the literature. For example, Lord Rayleigh has proposed a formula for the frequency of axisymmetric capillary wave oscillations of spherical drops through the balance of surface tension and inertial forces, almost two centuries ago<sup>12</sup> (for a discussion on Rayleigh modes, free and constrained, see Refs 8, 13–15), while Lord Kelvin<sup>16</sup> and Lamb<sup>17</sup> considered oscillations balancing inertia and gravity. The focus of those investigations has been to theoretically describe the ordinary frequency of surface oscillation modes in various frameworks, which can be classified based on the restoring force for oscillations, such as surface tension or gravity. A closely related concept is that of droplets on inclined substrates,<sup>18–20</sup> where it has been demonstrated that liquid drops on an inclined plane, oscillating vertically are even able to climb uphill.<sup>19,21</sup>

Despite a persistent interest in droplets on vibrating substrates and their technological implications, there are only a handful of studies in this area. They have employed experimental and theoretical methods to mainly describe the various modes of droplet surface-oscillations.<sup>22–35</sup> In particular, Becker *et al.*<sup>22,23</sup> have highlighted the role of nonlinear effects, for example, concerning the dependence of the oscillation frequency on the amplitude, as well as an asymmetry of the oscillation amplitude and interaction between the different oscillatory modes. Their experiments and theoretical analysis have indicated that the full theoretical description of droplet oscillations

is much more complex than suggested by the analysis above,<sup>11</sup> and that linear approximations are only relevant for small amplitude due to viscous damping. The nonlinear frequency response of oscillations of sessile droplets subjected to horizontal vibrations has also been the topic of a more recent study.<sup>24</sup> By means of experiments, it has been found that the droplet oscillates at a response frequency a multiple of the excitation frequency, but, only, for a sufficiently high vibration amplitude and a lower excitation frequency than the natural frequency of the sessile droplet. Moreover, at higher excitation frequency, the droplet oscillates at around the excitation frequency, while at ultrasonic excitation frequency, the droplet cannot follow the excitation. There is therefore a physical limitation for forming infinite modes of infinite wavenumber on the surface of a small droplet.

Besides those investigations, further understanding of droplet oscillations on vibrating substrates still remains elusive in the literature. In the case of experiments, this is mainly due to the fact that experimental studies face limitations when attempting to capture the various modes by tracking the surface oscillations of the drops or when trying to obtain information on the velocity patterns within the droplets. This practically means that there is a limited number of possible experimental pathways that can be taken to investigate these dynamic phenomena. One must assume that patterns will remain periodic, while, at the same time, data can depend strongly on a whole set of parameters (such as substrate roughness and evaporation), that are generally difficult to control and may vary between different experiments. With most research remaining focused on identifying the modes of the oscillating droplet surface, even the characterization of the natural modes has thus far had an incomplete degree of success.<sup>15,34–38</sup> For example, the concept of coinciding frequency with one of the natural frequencies has theoretically been used to model droplet oscillations.<sup>14,24,27,32,39–42</sup> In this case, a nonlinear mass–spring–damper, known as a Duffing oscillator,<sup>39</sup> has usually been employed to investigate axisymmetric modes of a sessile droplet due to vertical vibrations.<sup>32</sup> In other words, theory has predominantly been based on a mathematical analysis that includes various model assumptions, such as the type of restoring force, without taking into account the complex nature of oscillation phenomena, such as the flow within the droplets, the liquid–vapor coexistence, evaporation and physical pinning. Many of these assumptions are highly nonlinear, and despite efforts,<sup>24</sup> disentangling the interplay of the various parameters that determine the droplet behavior still remains a challenge. These experimental and theoretical limitations therefore point to evident gaps in our understanding of a fundamental phenomenon in nature. One that, moreover, is highly relevant for practical applications.

In view of these limitations, a possible way forward concerning the investigation of non-axisymmetric droplet oscillations on vibrating substrates would be the use of molecular-level methods based on suitable force-fields, such as molecular dynamics.<sup>43</sup> In this case, there is a need to reach an adequately large droplet size, such to allow for clear oscillation observations, flow fields, and possibly phase transitions, which naturally renders coarse-grained models the ‘go-to’ option.<sup>44</sup> However, again, simulating droplets of that size and carrying out a full investigation of droplet oscillation phenomena directly via this method is computationally costly, if not prohibitive, since it entails the investigation of a range of different droplet sizes to assess finite-size effects, as well as the exploration of parameters such as the frequency and amplitude of the oscillations for various substrate-wettability scenarios. Moreover, such models generally do not capture well some hydrodynamic effects or lack precise predictive power for some of the liquid properties, such as dynamic viscosity. These properties are required to be described correctly due to the competition of viscous and surface-tension forces, where the latter can act as the restoring force of the droplet shape.

Therefore, we have chosen to use the method of many-body dissipative particle dynamics (MDPD) in this study, which is a method that can easily handle large droplets and, moreover, can take into account hydrodynamic effects.<sup>6,45</sup> At the same time, suitable interactions can be obtained for a range of different compounds, including complex fluids beyond pure water droplets, which will specifically be investigated in this work.<sup>46</sup> In addition, the method includes thermal fluctuations and as a particle-based method provides the necessary molecular resolution for acquiring much needed information on both structural and dynamic properties of the droplets, while viscosity and surface tension are accurately reproduced by the model for the liquid of choice. In this context, MDPD has been used to successfully investigate the breakup of various liquids with a technologically relevant spectrum of Ohnesorge numbers (ratio of viscous to surface tension forces). The breakup is caused by surface-tension instabilities initiated by thermal fluctuations<sup>6</sup>. Importantly, the MDPD method does not require any *ad hoc* model assumptions, such as a contact-angle model, in the study of droplet oscillations, which could often be the case in continuum models.

Hence, by harvesting the advantages of the MDPD method, we have embarked here on investigating oscillating water droplets on horizontally vibrating solid substrates. A relevant range of simulation parameters has been considered for the amplitude and frequency of those vibrations while taking into account droplets of various sizes. In the simulations, we were able to characterize

in detail both the properties of droplets for the static case, as well as the properties during substrate vibrations. The static case is without substrate vibrations, and is used as a reference, for example, to determine the natural frequency of the droplets and the equilibrium contact angles. Here, one of the advantages of our method is the tight control of the experimental conditions during the simulation and the ability to track the instantaneous velocity and position of each particle at every simulation time-step. In this way, properties such as the shape of the droplet, its natural frequency, the receding and advancing contact angles, and especially the flow field during oscillations can be obtained as a function of time and with a molecular-level resolution. A key outcome of our research is the classification of the various scenarios of the droplets' behavior, identifying whether they lead to droplet breakup, together with an unraveling of the mechanisms associated with each of them. This internal mechanics has largely remained unknown, due to the limitations of previous methods. With regard to internal mechanisms, a parallelism with droplet breakup phenomena might be of relevance.<sup>6</sup>

In the following section, we provide details on our model and methods used in our investigations. Then, we present our results for both static and oscillating droplets in Section III, while we draw our conclusions and pave the way for future work in this area in Section IV.

## II. MODEL AND METHODOLOGY

Many-body dissipative particle dynamics is a particle-based simulation method that evolved from dissipative particle dynamics<sup>47,48</sup> and it incorporates both attractive and repulsive interactions. This enables the simulation of fluids with free surfaces, making it particularly well-suited for modeling liquid–vapor interfaces,<sup>49,50</sup> such as liquid droplets surrounded by vapor. In the case of MDPD, the equation of motion (Eq. 1) is integrated for each particle,  $i$ , which interacts with other particles,  $j$ , by means of a conservative force,  $\mathbf{F}^C$ , a random force,  $\mathbf{F}^R$ , and a dissipative force,  $\mathbf{F}^D$ . In our work, the integration of the equations of motion is realized via a modified velocity-Verlet algorithm<sup>51</sup> with a time-step,  $\Delta t = 0.005$  (MDPD units), as implemented in LAMMPS software<sup>52</sup>, with the equation reading

$$m \frac{d\mathbf{v}_i}{dt} = \sum_{j \neq i} \mathbf{F}_{ij}^C + \mathbf{F}_{ij}^R + \mathbf{F}_{ij}^D. \quad (1)$$

The mathematical expressions of the conservative force reads

$$\mathbf{F}_{ij}^C = A \omega_c(r_{ij}) \mathbf{e}_{ij} + B (\bar{\rho}_i + \bar{\rho}_j) \omega_d(r_{ij}) \mathbf{e}_{ij}. \quad (2)$$

Here,  $A < 0$  is the attractive strength of the force, while  $B > 0$  is a repulsive interaction strength. The repulsive force also depends on the local density and includes many-body effects. The repulsive parameter,  $B$ , has to be the same for all the interactions due to a known ‘no-go’ theorem<sup>53</sup>, otherwise the force wouldn’t be conservative.  $r_{ij}$  is the distance between particles, while  $e_{ij}$  is the direction vector from particle  $i$  to particle  $j$ .  $\omega_c(r_{ij})$  and  $\omega_d(r_{ij})$  are weight functions that are defined as follows:

$$\omega_c(r_{ij}) = \begin{cases} 1 - \frac{r_{ij}}{r_c}, & r_{ij} \leq r_c \\ 0, & r_{ij} > r_c, \end{cases} \quad (3)$$

$$\omega_d(r_{ij}) = \begin{cases} 1 - \frac{r_{ij}}{r_d}, & r_{ij} \leq r_d \\ 0, & r_{ij} > r_d. \end{cases} \quad (4)$$

Here, the cutoff distance for the attractive interaction is denoted with  $r_c$  and is set to unity. The repulsive-interaction cutoff is  $r_d = 0.75r_c$ .<sup>54</sup> The many-body contributions in the repulsive force expressed through the local densities,  $\bar{\rho}_i$  and  $\bar{\rho}_j$ , are calculated as follows:

$$\bar{\rho}_i = \sum_{j \neq i} \frac{15}{2\pi r_d^3} \left(1 - \frac{r_{ij}}{r_d}\right)^2. \quad (5)$$

Thermal fluctuations are taken into account through random and dissipative forces in the equation of motion (Eq. 1), which act as the thermostat of the particles (the temperature is  $T = 1$  in MDPD units for static droplets). These are expressed as

$$\mathbf{F}_{ij}^D = -\gamma_D \omega_D(r_{ij}) (\mathbf{e}_{ij} \cdot \mathbf{v}_{ij}) \mathbf{e}_{ij}, \quad (6)$$

$$\mathbf{F}_{ij}^R = \sigma_R \omega_R(r_{ij}) \xi_{ij} \Delta t^{-1/2} \mathbf{e}_{ij}. \quad (7)$$

Here,  $\gamma_D$  is the dissipative strength,  $\sigma_R$  the strength of the random force,  $\mathbf{v}_{ij}$  the relative velocity between particles, and  $\xi_{ij}$  a random variable from a Gaussian distribution with zero mean and unit variance. In addition,  $\gamma_D$  and  $\sigma_R$  are related via the fluctuation–dissipation theorem,<sup>55</sup> in this case

$$\gamma_D = \frac{\sigma_R^2}{2k_B T}, \quad (8)$$

while the weight functions for the forces are

$$\omega_D(r_{ij}) = [\omega_R(r_{ij})]^2 = \left(1 - \frac{r_{ij}}{r_c}\right)^2. \quad (9)$$

To simulate water droplets, the commonly adopted values for water in MDPD have been used, *i.e.*  $A = -40$  and  $B = 25$  (MDPD units),<sup>45,56</sup> while the dissipative coefficient is  $\gamma_D = 4.5$ .<sup>57,58</sup> The conversions from reduced to real units for the particle properties based on this model are reported in Table I.

To prepare the simulation for investigating the droplet oscillations (both natural ones and those caused by the vibrating substrate), freely suspended droplets of different sizes were first equilibrated in a simulation box with dimensions  $L_x = 1200$ ,  $L_y = 220$ , and  $L_z = 120$  (MDPD units). The total number of particles in the simulation were  $N = 5 \times 10^4$ ,  $N = 10 \times 10^4$ , or  $N = 20 \times 10^4$  particles, which correspond to spherical droplets with radii  $R = (\frac{3N}{4\pi\rho})^{1/3} = 12.54, 15.80$  and  $19.91$  (MDPD units), respectively. For the larger droplets with  $N \geq 10 \times 10^4$ , key properties for the droplets, such as the contact angle of the droplet, seem not to depend on the droplet size.<sup>59</sup> To maintain the same thermodynamic conditions given the number of particles and the temperature of the system, we keep the volume available to the water particles the same by means of implicit walls, with further details on these walls given later. Each droplet, which consists of slightly less than  $N$  particles due to evaporation, was placed in the middle of the simulation box at position  $(x = 0, y = 0)$  and on a smooth, unstructured, solid substrate (at  $z = 10$ ) (Figure 1). This substrate was implicitly modeled via the Lennard-Jones (LJ) potential,<sup>60</sup> mathematically expressed as follows:

$$U^{9-3}(z') = 4\epsilon_{ws} \left[ \left( \frac{\sigma_{ws}}{z'} \right)^9 - \left( \frac{\sigma_{ws}}{z'} \right)^3 \right]. \quad (10)$$

TABLE I: Relation between MDPD units and real units. The scaling is done by matching surface tension  $\gamma$  and density of water  $\rho$  to values measured from MDPD simulations using  $A = -40$  and  $B = 25$ . The coarse-graining level is defined so that one MDPD particle represents three water molecules.

Parameter	MDPD value	Real value
Particle	1	3 H <sub>2</sub> O
$r_c$	1	8.17 Å
$\rho$	6.05	997 kg/m <sup>3</sup>
$\gamma$	7.62	72 mN/m

Hence, the force included in the equations of motion for each particle that interacts with the substrate when its distance is below the LJ cutoff,  $r_{\text{LJ}} = 1.0$ , is obtained to be  $F_{\text{ws}} = -\frac{\partial U^{9-3}(z')}{\partial z'}$ . Here,  $z'$  is the distance between the liquid particles and the substrate,  $\sigma_{\text{ws}}$  is set to unity, while  $\epsilon_{\text{ws}}$  is a parameter used to tune the affinity of the droplet to the substrate, thus controlling the equilibrium contact angle of the droplet. The values  $\epsilon_{\text{ws}}$  chosen were droplet-size-dependent. For  $N = 20 \times 10^4$ , the exact values of the interaction strength used were  $\epsilon_{\text{ws}} = 3.0, 2.5, 2.0, 1.0$ , and  $0.1$ , which correspond to contact angles  $\theta = 50^\circ, 65^\circ, 90^\circ, 115^\circ$ , and  $140^\circ$ , respectively. For  $N = 10 \times 10^4$ ,  $\epsilon_{\text{ws}} = 3.5, 3.0, 2.0, 1.0, 0.1$  for the same corresponding angles; for  $N = 5 \times 10^4$ ,  $\epsilon_{\text{ws}} = 3.5, 3.0, 2.0, 1.0, 0.25$ , respectively. Overall,  $\epsilon_{\text{ws}}$  was chosen such to produce the same equilibrium contact-angles for all sizes of droplets. This range of contact-angles cover hydrophilic and hydrophobic substrate cases, which are relevant experimentally.<sup>33</sup> A perspective and orthogonal view of a sessile droplet for the static substrate case with equilibrium contact angle  $90^\circ$  are presented in Figure 1, while typical measurements of the contact angle are presented in Figure 2. In the case shown, the standard deviation of the contact angle measurements in a single trajectory are of the order of  $2^\circ$ . Finally, a purely repulsive LJ wall was used to prevent particles from escaping from the top of the simulation box and sticking to the bottom substrate from below, due to the presence of periodic boundary conditions on all sides of the simulation box.

To determine the contact angle, we use a polynomial method up to order  $n$  to obtain the surface curvature of the  $y = 0$  cross-section of the droplet (like the lower panel of Figure 1), given by

$$x = p(z) = p_1 z^n + p_2 z^{n-1} + \dots + p_n z + p_{n+1}, \quad (11)$$

where  $p_n$  are the coefficients obtained from least-squares fitting. In the simulations, values of  $3 \leq n \leq 5$  best fit the surface profile. The contact angle is then determined from the tangent line of the polynomial function (Equation 11) at the droplet contact-line as shown in Figure 1. Since the stationary droplet is generally axisymmetric along the  $z$  direction, two contact angles were measured along the  $x$  direction (on the  $x - z$  plane) to improve statistical accuracy for the stationary droplet instead of one required based on a sufficient number of statistically independent ensemble droplet-snapshots. We will later acquire separate measurements of the advancing and receding contact angles when substrate vibrations in the  $x$  direction are activated. In this work, we use the notation  $\theta_1$  and  $\theta_2$  instead of the more common notation  $\theta_r$  and  $\theta_a$  for the receding and advancing contact-angles, respectively. This choice reflects the alternating nature of the angles for oscillating droplets on a vibrating substrate. Thus, the left angle (toward the negative  $x$  axis) will

always be denoted as  $\theta_1$ , while the right angle (in the positive  $x$  direction) will be denoted as  $\theta_2$ , as shown in Figure 1.

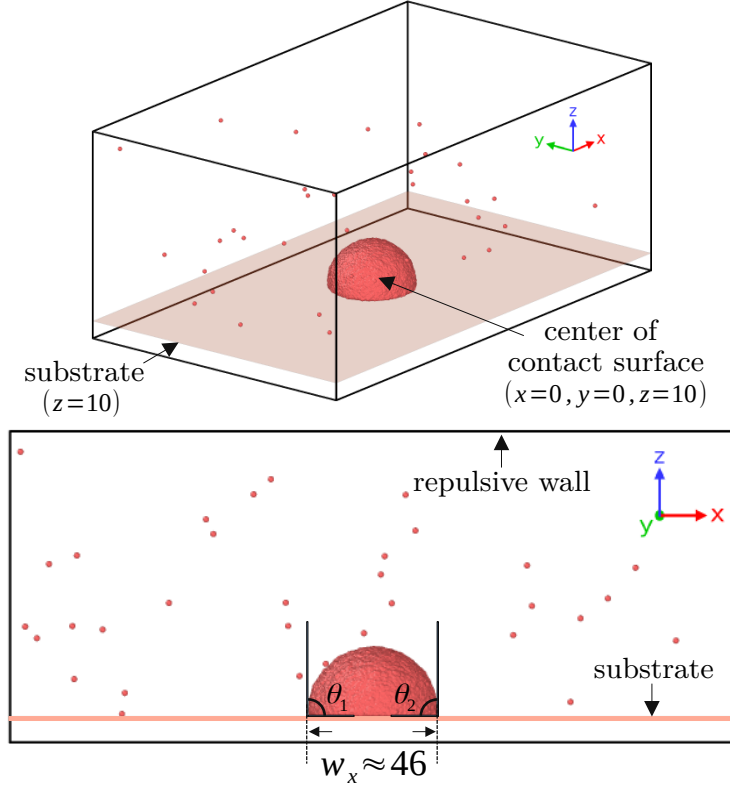


FIG. 1: A typical snapshot in the simulations of a water droplet on a static substrate. In the lower panel,  $\theta_1$  and  $\theta_2$  indicate the contact angles of the droplet at the two points along the contact line, as indicated. Here, the number of particles  $N = 20 \times 10^4$  and the droplet–substrate affinity  $\epsilon_{ws} = 2.0$ , resulting in equilibrium contact angles  $\theta_1, \theta_2 \approx 90^\circ$ . The droplet width at the static contact surface is  $w_x \approx 46$ . Snapshots were generated using OVITO software.<sup>61</sup>

To induce the droplet oscillations, the substrate is vibrated non-axisymmetrically, in our case in the  $x$  direction. The characteristics of the substrate vibration, *i.e.* the amplitude and the frequency of the oscillation, are set as inputs to the simulation and remain constant throughout. The instantaneous velocity of the substrate, is given by:

$$u_{\text{sub}}(t) = -A_{\text{sub}} \omega_{\text{sub}} \sin(\omega_{\text{sub}} t). \quad (12)$$

$A_{\text{sub}}$  is the vibration amplitude, and  $\omega_{\text{sub}} = 2\pi f_{\text{sub}}$  the angular frequency, with  $f_{\text{sub}}$  the vibration frequency. The range of parameters used for the substrate vibrations, has been chosen to be in the

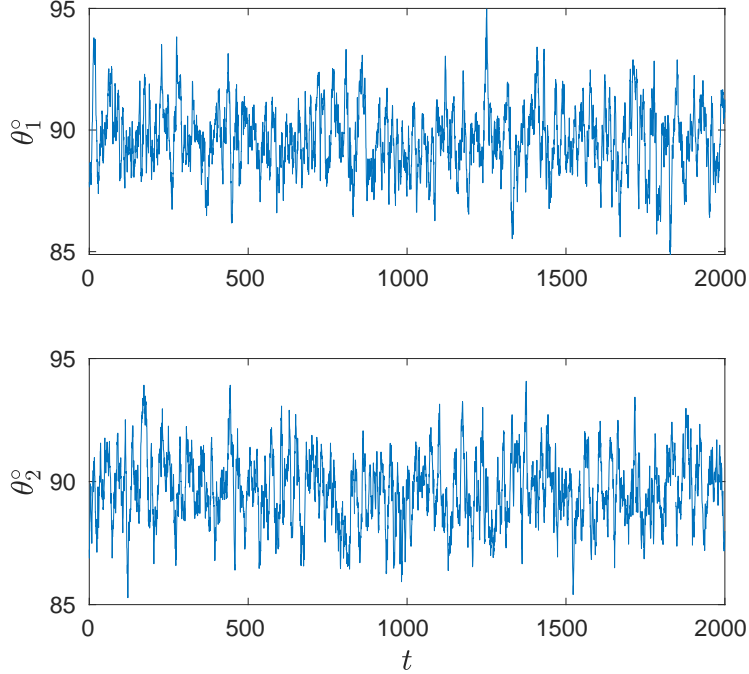


FIG. 2: Contact angles  $\theta_1$  and  $\theta_2$  of a static droplet over simulation time,  $t$ . Same parameters as in Figure 1 where  $N = 20 \times 10^4$  and  $\epsilon_{ws} = 2.0$ . The values shown above are averages from four samples. The contact angles are about  $90^\circ$ .

vicinity of the natural oscillation frequency of the droplets determined from our simulations and experiments,<sup>33</sup> specifically  $225 \leq A_{\text{sub}} \leq 900$  and  $3.75 \times 10^{-3} \leq f_{\text{sub}} \leq 15 \times 10^{-3}$  (MDPD units).

It is important to relate our explicit  $\sim 10\text{nm}$  radius droplets to droplets with macroscopically observable size. This can be carried out since it is known that the larger droplets are already in the appropriate scalable regime.<sup>59</sup> The characteristic inertial timescale of a droplet can be estimated as  $t_c = \sqrt{\frac{\rho R^3}{\gamma}}$ . For the droplet with  $N = 20 \times 10^4$  and  $R = 19.91$ , this yields  $t_c = 79.16$  (MDPD unit). For a macroscopic droplet with a radius of  $R^{\text{real}} = 1\text{mm}$  (where the superscript "real" denotes real values in SI units of droplets scaled to macroscopic sizes), we obtain  $t_c^{\text{real}} = \sqrt{\frac{\rho^{\text{real}} (R^{\text{real}})^3}{\gamma^{\text{real}}}} = 3.72 \times 10^{-3}\text{s}$ . The oscillation frequency of the substrate in "real" macroscopic droplet units can then be estimated, where  $f_{\text{sub}}^{\text{real}} = f_{\text{sub}} t_c / t_c^{\text{real}}$ . For example, for a droplet with a radius of  $1\text{mm}$ , the corresponding frequency is approximately  $80\text{Hz} \lesssim f_{\text{sub}}^{\text{real}} \lesssim 320\text{Hz}$ . Here  $A_{\text{sub}}$  is the vibration amplitude for the smooth and unstructured surface where friction is not included in the simulations; hence, the real oscillation amplitude of the substrate,  $A_{\text{sub}}^{\text{real}}$ , is estimated based on the oscillation amplitude of the mean particle  $x$  position at the contact surface,  $x_{\text{cs}}$ . Using the scaling relation  $A_{\text{sub}}^{\text{real}} = x_{\text{cs}} R^{\text{real}} / R$ , we obtain  $0.5\text{mm} \lesssim A_{\text{sub}}^{\text{real}} \lesssim 4\text{mm}$ .

To conduct our investigations, a droplet is initially equilibrated on the substrate until the standard deviation of the contact angles,  $\sigma_{\theta_1}$  and  $\sigma_{\theta_2}$ , are of the order of  $2^\circ$ . A snapshot of the droplet at relaxation equilibrium is as shown in Figure 1. Vibrations are then activated only after the droplet has reached equilibrium. The simulation duration varies depending on the observed droplet behavior, ensuring that the set of observed phenomena are not truncated by an insufficient timescale of the simulation. Consequently, the typical simulation time for vibrating substrates ranges from  $5000 \leq t \leq 10000$  (MDPD units, natural for the model). We shall note here that for the case of molecular dynamics simulations of physics-based models based on a similar equation of motion, the corresponding times in terms of natural units in the model would be significantly longer.<sup>62</sup> Therefore, computation time would grow accordingly. Average properties in static cases were calculated from an ensemble of statistically independent configurations (typically four), while dynamic properties such as flow fields were continuously monitored and estimated using a running average of typically four consecutive configurations, obtained at a suitable short-time interval during the simulation, namely  $t_{\text{int}} = 7.5$ .

### III. RESULTS AND DISCUSSION

#### A. Droplet on a static substrate

Droplets were investigated on static substrates to determine various reference properties, including the wettability of the substrate through the equilibrium contact angle. A key property in the context of this study is the natural eigenfrequency of the droplets, which depends on both the droplet size and substrate wettability. In our case, this can be measured not only by tracking the surface oscillations, but, also, oscillations of the center-of-mass of the droplet individually in all Cartesian directions, as well as the collective motion of the particles in these directions. Previous studies have employed methods such as principal component analysis (also, known as principal orthogonal decomposition) to determine the droplet eigenfrequencies based on droplet surface oscillations.<sup>32</sup> However, these methods are computationally expensive for droplets with tens of thousands of particles, like what we have here.

We find that measuring the values of  $z_{\text{com}}$ , the center-of-mass of the droplet in the  $z$  (away from the substrate) direction, over time and applying a Fourier transform to these data (Figure 3) provides accurate results for the main natural eigenmodes of the droplets. The lateral droplet

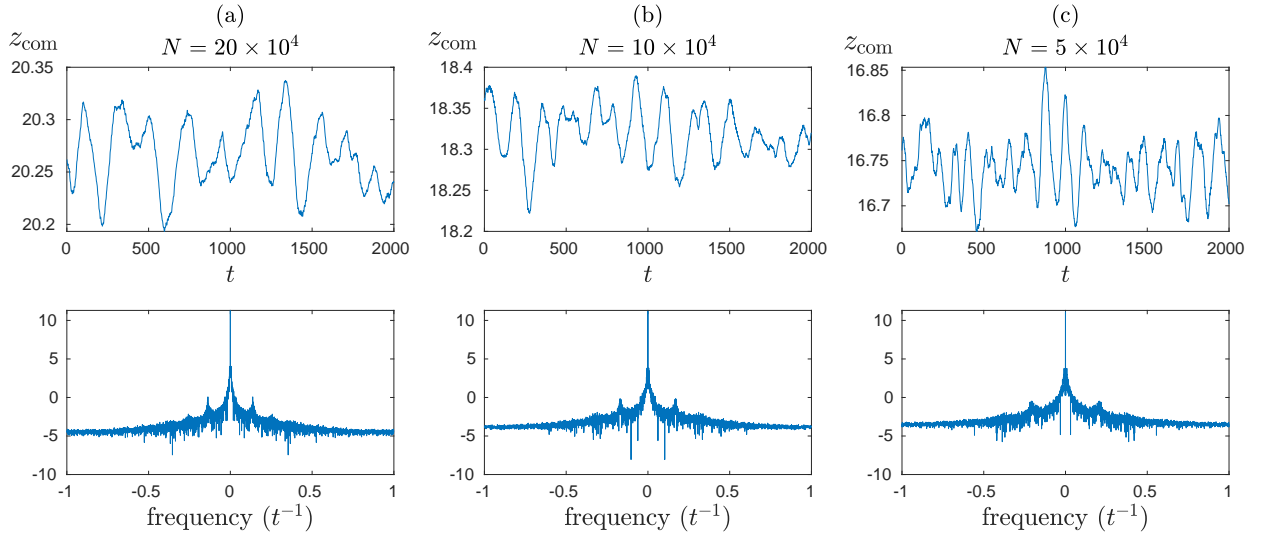


FIG. 3: Static droplet analysis for: (a) Number of particles  $N = 20 \times 10^4$ , (b)  $N = 10 \times 10^4$  and (c)  $N = 5 \times 10^4$ , with contact angles  $\theta = 90^\circ$ . Upper panels: The center-of-mass position ( $z_{\text{com}}$ ) of the static droplet over time  $t$ . Lower panels: Fourier analysis of  $z_{\text{com}}$  in natural log scale vertically. Three eigenmodes are observed in each case (a), (b), and (c). For (a) the frequencies of the eigenmodes are  $(t^{-1}) \sim \pm 0.0052, \pm 0.14$  and  $\pm 0.26$ ; (b)  $\sim \pm 0.0057, \pm 0.17$  and  $\pm 0.32$ ; (c)  $\sim \pm 0.0067, \pm 0.20$  and  $\pm 0.37$ . All results are obtained from an average of four different runs.

oscillations in the  $x - y$  plane yield the same results as  $z_{\text{com}}$ , indicating that the lateral and vertical oscillation modes of the droplet are entirely interrelated. A similar conclusion has been drawn when the droplet eigenfrequencies were calculated based on all particle coordinates, albeit noise in the data was slightly higher in this case due to the thermal fluctuations of the particles and the different environment between particles in the bulk and the interfaces.

From the eigenfrequency measurements for a droplet with a size of about  $N = 20 \times 10^4$  and a contact angle  $\theta = 90^\circ$ , we find that the 1<sup>st</sup> natural oscillation mode corresponds to a low frequency  $\pm 0.0052$ , and two higher characteristic frequencies for the 2<sup>nd</sup> and 3<sup>rd</sup> natural oscillation modes at  $\pm 0.14$  and  $\pm 0.26$ , respectively. The 3<sup>rd</sup> weaker eigenmode occurs at approximately double the frequency of the 2<sup>nd</sup> eigenmode (Figure 3(a)). This indicates that nonlinear effects are indeed present during sessile droplet oscillations, possibly due to the presence of thermal fluctuations. Using the relation  $f^{\text{real}} = f t_c / t_c^{\text{real}}$  for the natural frequency,  $f$ , and assuming a droplet with a real spherical radius of 1mm, these values correspond to natural oscillation modes of  $\sim 110\text{Hz}$ , 3kHz

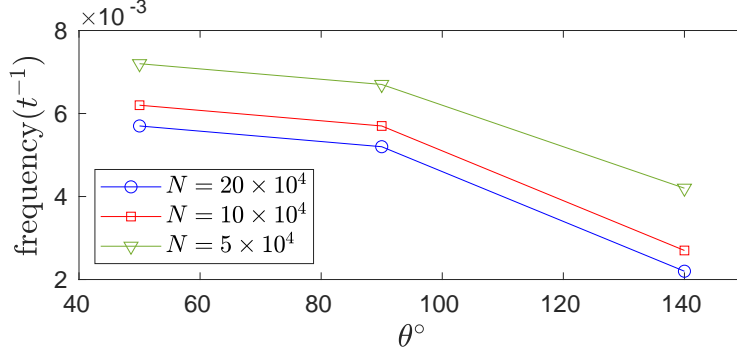


FIG. 4: Frequency of the 1<sup>st</sup> oscillation mode for static droplets with number of particle  $N = 5 \times 10^4$ ,  $N = 10 \times 10^4$  and  $N = 20 \times 10^4$ , each with contact angles  $\theta = 50^\circ$ ,  $90^\circ$  and  $140^\circ$ .

All results are obtained from an average of four different runs.

and 5.5kHz. In addition, we observe that the natural eigenmodes shift slightly in smaller droplets, with frequencies of the modes increasing moderately ( $\sim 20\%$ ) each time the number of particles is reduced by half (Figures 3(b) and 3(c)). This is in line with the rule of thumb that frequency is inversely proportional to object size, since  $(0.5)^{1/3} \approx 0.8$ . For droplets with a contact angle of  $\theta = 140^\circ$ , across all three sizes  $N$ , the frequency spectrum is dominated by the 1<sup>st</sup> low-frequency mode, while the 2<sup>nd</sup> and 3<sup>rd</sup> modes are not observed in the Fourier analysis. We compared the 1<sup>st</sup> mode at various contact angles  $\theta$  for droplets of all three sizes (Figure 4). The 1<sup>st</sup> natural oscillation mode increases non-linearly with increasing wettability for all tested droplet sizes, and the frequency change of the 1<sup>st</sup> mode is less pronounced for hydrophilic surfaces. Overall, the natural eigenfrequency of the droplets leads to a variation in  $z_{\text{com}}$  of approximately  $\lesssim 1\%$  across all three sizes.

## B. Droplet oscillation

Having determined the natural frequency of the droplets across our range of droplet sizes and substrate wettability, we took the next steps to investigate the various scenarios unfolding for the oscillating droplets when substrate vibrations were activated. Our results for different amplitude and frequency ranges are summarized in Figure 5 for droplets with  $N = 20 \times 10^4$  MDPD particles, while results for smaller droplets are provided in the Supplementary Material (SM). The behavior of the smaller droplets very much follows the same qualitative trends, therefore in what follows we describe the  $N = 20 \times 10^4$  case and concentrate on that.

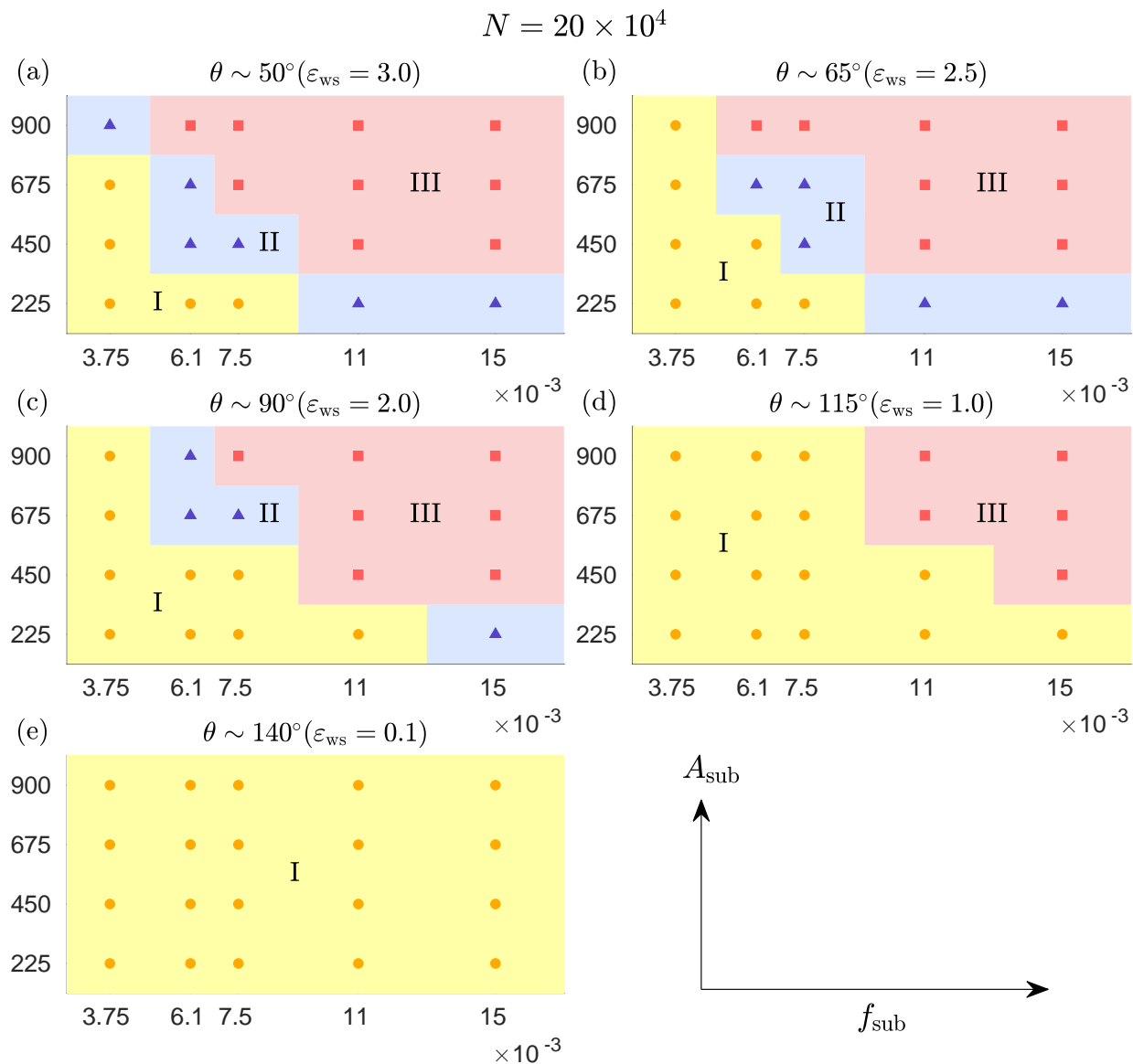


FIG. 5: State diagram showing Phase I, II, and III, indicated by different color shading (see text for details), as a function of the amplitude and frequency of substrate vibrations for a droplet with  $N = 20 \times 10^4$ . Each plot corresponds to a substrate with different wettability, with the equilibrium contact angle,  $\theta$ , of the droplet on a static substrate (without vibrations) indicated at the top of each plot: (a)  $\theta \sim 50^\circ$ ; (b)  $\theta \sim 65^\circ$ ; (c)  $\theta \sim 90^\circ$ ; (d)  $\theta \sim 115^\circ$ ; (e)  $\theta \sim 140^\circ$ .

The most trivial scenario occurs when the droplet exhibits symmetric oscillations. That is, oscillations repeat periodically with the same period as the substrate vibrations given by Equation 12. This occurs always within our range of parameters for the substrate with a contact angle  $\theta = 140^\circ$ . In this case, the droplet remains stable with no breakup of the droplet occurring at any

time during the simulations, which is confirmed by running multiple, different trajectories with different initial velocity seed over extended times. This scenario will be named here as ‘Phase I’, and the characteristics of such oscillations will be described in detail later.

As the substrate wettability increases (Figure 5(d)), though the substrate still remains hydrophobic ( *i.e.*,  $\theta = 115^\circ$ ), a different droplet behavior emerges at high amplitude and frequency of substrate vibration. In particular, at lower oscillation amplitudes, the Phase I scenario persists regardless of vibration frequency. However, as the frequency  $f_{\text{sub}}$  and amplitude  $A_{\text{sub}}$  increase, ‘Phase III’ emerges, where the immediate breakup of the droplet takes place as a result of the vibrations. Details regarding the breakup will be discussed in later sections.

For substrates with an equilibrium contact angle  $\theta = 90^\circ$ , ‘Phase II’ scenario appears in our simulations at high oscillation frequency and amplitudes (Figure 5(c)). In Phase II, the droplet exhibits symmetric oscillations for a prolonged time before an asymmetry in the oscillations arises, leading to the breakup of the droplet. We observe that Phases II and III are more prevalent than Phase I droplet oscillations for the range of frequencies and amplitudes considered here. In particular, Phase III again emerges at higher oscillation amplitudes and frequencies, while Phase II appears along the boundary between Phase I and III. When the equilibrium contact angle becomes less than  $90^\circ$ , Phase III occurs at even lower frequencies and amplitudes (Figure 5(a) and (b)). However, there appear to be threshold values for both frequency and amplitude even at smaller contact angles. In particular, Phase I is observed consistently in all cases when the frequency is below  $7.5 \times 10^{-3}$  and amplitude below 675. The state diagrams for smaller droplets presented in Supplementary Material reveal similar trends, with Phase II appearing more prominently along the boundary between Phase I and III, and conditions for droplet breakup being more favorable. This is an indication that surface-tension forces, which are more dominant in smaller droplets due to increased surface-area-to-volume interactions would promote the droplet breakup. Overall, the breakup of the droplets is favored by higher amplitudes and frequencies, especially for droplets on hydrophilic substrates with smaller contact angles. Details for the characteristics of both Phase II and Phase III will be discussed in the following subsections.

### ***1. Phase I oscillation***

Having provided the global picture from our simulations, we now proceed with discussing the details of each scenario. Overall, the simulated properties in Phase I clearly reflect those observed

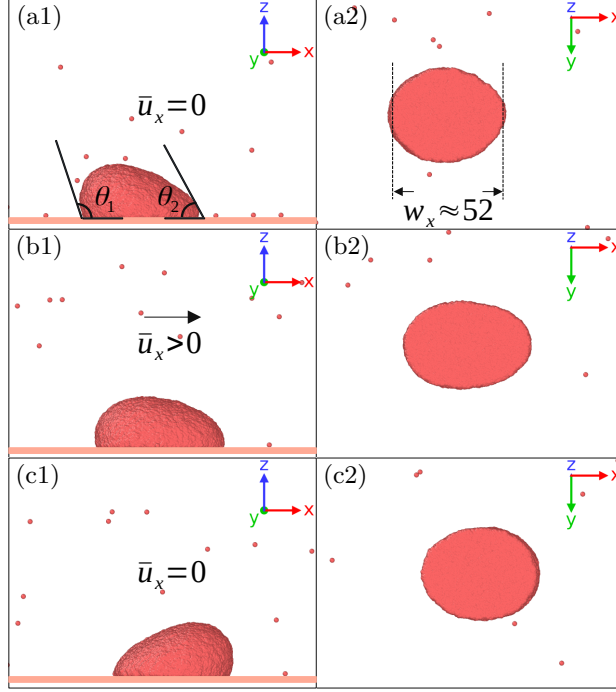


FIG. 6: Example of Phase I oscillation, with time progressing from (a) to (c).  $N = 20 \times 10^4$ ,  $\varepsilon_{ws} = 2.0$  ( $\theta = 90^\circ$ ),  $A_{\text{sub}} = 900$ ,  $f_{\text{sub}} = 3.75 \times 10^{-3}$ .  $\bar{u}_x$  indicates the mean velocity of the droplet along the oscillation direction  $x$ . (a1) Side view; (a2) bottom view at the contact surface, taken at the same moment as (a1). (b1, b2) Side and bottom views taken one-quarter of the oscillation period after (a). (c1, c2) Side, bottom views taken one-quarter of the oscillation period after (b).

in oscillation experiments, where breakup is avoided.<sup>33</sup> Hence, they rather correspond to trivial droplet oscillation cases, which, however, can be investigated in greater detail with MDPD than in experimental measurements. Figure 6 illustrates typical snapshots of Phase I oscillations, which are periodic over time without leading to droplet breakup. In the example shown in Figure 6, the droplet contains  $N = 20 \times 10^4$  particles, with equilibrium contact angles  $\theta_1, \theta_2 \approx 90^\circ$  (*i.e.* droplet–substrate affinity  $\varepsilon_{ws} = 2.0$ ), an oscillation amplitude  $A_{\text{sub}} = 900$ , and frequency  $f_{\text{sub}} = 3.75 \times 10^{-3}$ . Panels (a) and (c) of Figure 6 correspond to droplet configurations at times in which the maximum difference between angles  $\theta_1$  and  $\theta_2$  is attained. At these moments, the total velocity (moment) of the droplet in the  $x$  direction becomes zero. In contrast, panels (b) of Figure 6 illustrate a typical droplet conformation when the droplet has reached its maximum speed.

The above observations can be quantified by monitoring various properties, such as the center-of-mass of the droplet,  $x_{\text{com}}$ , its width,  $w_x$ , the dynamic contact angles,  $\theta_1$  and  $\theta_2$ , and the contact surface area,  $A_{\text{cs}}$ , of the droplet, which are compiled in Figure 7. These properties are compared

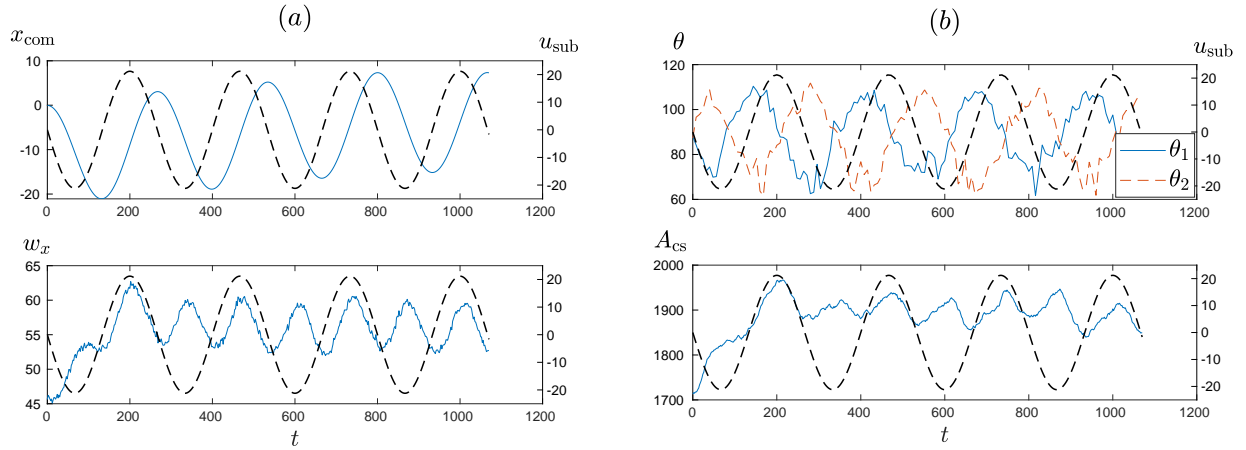


FIG. 7: Phase I oscillation for the droplet with  $N = 20 \times 10^4$ ,  $\varepsilon_{\text{ws}} = 2.0$ ,  $A_{\text{sub}} = 900$ ,  $f_{\text{sub}} = 3.75 \times 10^{-3}$ , shown in Figure 6. (a) Upper panel:  $x_{\text{com}}$ , center-of-mass of the droplet; Lower panel:  $w_x$ , width of the droplet in the  $x$  direction at the contact surface. (b) Upper panel:  $\theta_1$  and  $\theta_2$  contact angles; Lower panel:  $A_{\text{cs}}$ , contact surface area of the droplet. All shown in comparison with the substrate velocity  $u_{\text{sub}}$ , which is presented in the plots by dashed lines. All plots are obtained from a single simulation trajectory.

to the periodic motion of the substrate, in this case, its instantaneous velocity,  $u_{\text{sub}}$ . In particular, we can observe that  $x_{\text{com}}$  follows the periodic pattern of the substrate vibrations with a time lag of a quarter of the oscillation period, which persists over time during the simulation (Figure 7(a)). On the contrary, the width of the droplet  $w_x$  (the width in the  $x$  direction at the contact surface, placed at  $z = 10$ , as shown in Figure 6(a2)) closely follows the periodicity of the substrate velocity,  $u_{\text{sub}}$  (Figure 7(a)). In this case, the droplet obtains its maximum width in the  $x$  direction when the substrate velocity,  $u_{\text{sub}}$ , is also at its maximum, and the droplet relaxes towards its new forced equilibrium state (Panels (b) of Figure 6), resembling that of a droplet on a static substrate when its center-of-mass velocity is zero. This state is a little more spread out — the droplet never recovers the initial width of 45, oscillating around the natural width of 55 as long as the vibration remains on. In contrast, the droplet obtains its minimum width when the substrate velocity becomes instantaneously zero. At this point, the difference between angles  $\theta_1$  and  $\theta_2$  becomes maximum (Panels (a) and (c) of Figure 6). In particular, the contact angles of the droplet exhibit a stable periodic change, with a phase shift of a quarter of the oscillation period relative to

the substrate velocity (Figure 7(b)). For the droplet on a static substrate with a contact angle of about  $90^\circ$ , the receding angle is around  $62^\circ$  and the advancing angle is around  $110^\circ$ . The contact angles  $\theta_1$  and  $\theta_2$  alternatively reach the receding and advancing angles periodically. In this example, with droplet–substrate affinity  $\varepsilon_{ws} = 2.0$ , oscillation amplitude  $A_{\text{sub}} = 900$ , and frequency  $f_{\text{sub}} = 3.75 \times 10^{-3}$ , both angles return to  $90^\circ$  once per oscillation period when the amplitude of the substrate velocity,  $u_{\text{sub}}$ , reaches its maximum, as shown in the snapshot in Figure 6(b). This periodic pattern of contact angles can vary depending on the oscillation amplitude and frequency, as well as the wettability, determined by  $\varepsilon_{ws}$ . The contact surface area,  $A_{\text{cs}}$ , also shows periodic behavior, matching the changes in droplet width at the contact surface.

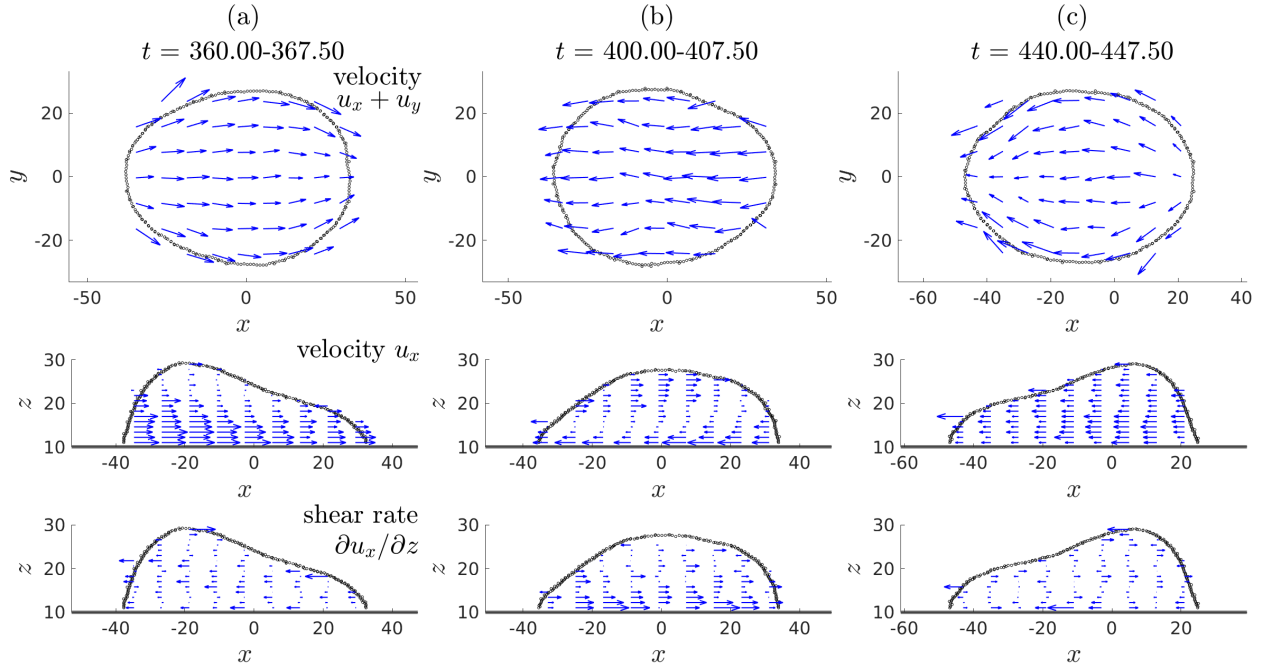


FIG. 8: Phase I oscillation for the droplet with  $N = 20 \times 10^4$ ,  $\varepsilon_{ws} = 3.0$  ( $\theta = 50^\circ$ ),  $A_{\text{sub}} = 225$ ,  $f_{\text{sub}} = 7.5 \times 10^{-3}$ . Upper panels: time-averaged velocity field at the contact surface for the time intervals (a)  $t = 360 \sim 367.5$ , (b)  $t = 400 \sim 407.5$ , (c)  $t = 440 \sim 447.5$ . Middle panels: time-averaged velocity field in the  $x$  direction at the cross-section at  $y = 0$ , over the same time intervals as the top row. Lower panels: time-averaged shear rate,  $\dot{\gamma} = \partial u_x / \partial z$ , obtained from averaging the consecutive shear rates. Each velocity field is time-averaged over four consecutive frames, with time-interval  $t_{\text{int}} = 7.5$ .

We have carefully analyzed the velocity profiles of the droplets by examining particle-velocity data for cross-sections of the droplet in various planes at each time and present representative

cases here. In Figure 8, which shows a different wetter case in phase I than Figures 6 and 7, now having  $N = 20 \times 10^4$ ,  $\epsilon_{ws} = 3.0$  (equilibrium contact angles  $\sim 50^\circ$ ),  $A_{\text{sub}} = 225$ ,  $f_{\text{sub}} = 7.5 \times 10^{-3}$ , such velocity profiles are plotted for cross-sections in the  $x - y$  and  $x - z$  planes. After evaluating the different profiles, we identified that the most representative profiles are those on the  $x - y$  and  $x - z$  planes for the velocity components  $(u_x, u_y)$  and  $u_x$ , respectively, as presented in Figure 8. In particular, the  $x - y$  cross-section is taken close to the contact surface and spans the entire droplet, while the  $x - z$  cross-section includes the entire droplet along the  $x$  direction. In addition to the velocity profiles, we have also determined the gradient of the velocity  $u_x$  with respect to the  $z$  coordinate, which reflects the shear rate  $\dot{\gamma}$  in the  $z$  direction. This analysis allows us to further understand the internal velocity distribution and shear dynamics within the droplet.

The results for Phase I droplet oscillations, illustrated in Figure 8 are taken at the specific times indicated by square and dot markers in Figure 9. The time trace in the latter figure (lower panel in subplot (a)) reveals that the mean velocity of the droplet,  $\bar{u}_x$ , here in this stronger wetting case, would follow that of the substrate velocity, regardless of the exact moment during the oscillation cycle at which these data are recorded. In contrast to the previous discussed Phase I system shown in Figure 6 and 7, where the droplet attains a symmetric shape similar to that of a static droplet when both the droplet and substrate velocities reach their maximums, in the current case shown in Figure 8 and 9, the droplet exhibits a symmetric shape resembling the static droplet when the velocities of both the droplet and substrate are around zero. In addition, the flow field is not uniform. The velocities in the  $x - y$  plane near the center of the droplet at  $y = 0$  tend to follow the direction of the vibration, with particle velocities aligning with the vibration direction. In contrast, particle velocities along the contact line tend to follow the outline of the droplet, especially when the droplet reaches one of its extrema during the oscillation cycle (Figure 8(a) and (c)).

In the case of the velocity field in the  $x - z$  plane and the shear rate, we observe periodic patterns with the largest shear rate as measured in the middle region ( $y = 0$ ) of the droplet at the contact surface,  $\dot{\gamma}_{\text{cs}}$ , occurring when both the substrate and droplet velocities are close to zero (Figure 9(b)). This corresponds to the droplet being at the oscillation extrema. In this case, the shear rate peaks, due to the changes in momentum as the droplet follows the vibrating substrate moving towards its center of oscillation. This moment is reflected in the symmetric shape of the droplet (Figure 8(b)). Moreover, the shear rate becomes zero when both the droplet and the substrate attain their maximum kinetic energy. In this case, the stresses arising from differences in the velocities of the particles are minimum near the contact surface, and the droplet obtains an

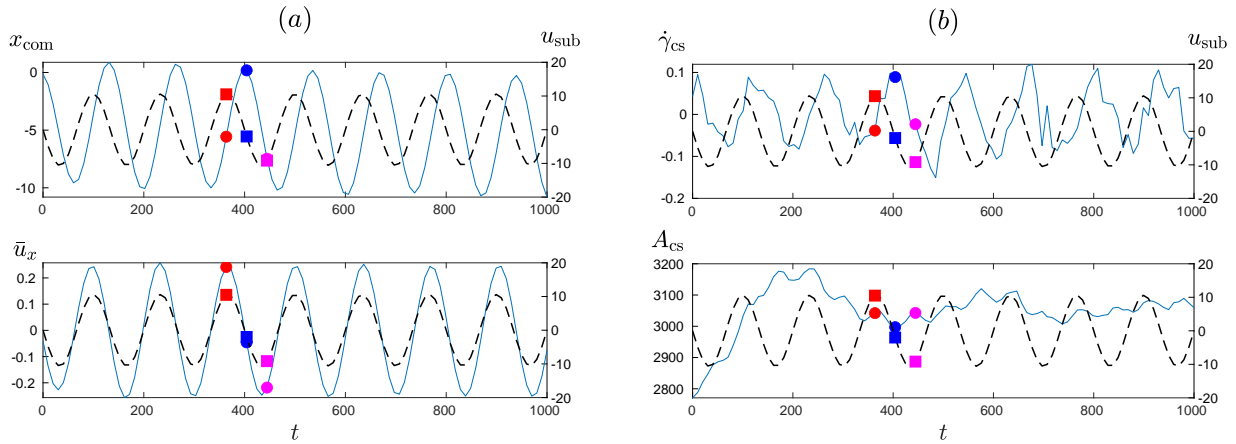


FIG. 9: Time sequence data for the droplet shown in Figure 8. (a) Upper panel: center-of-mass position of the droplet; Lower panel: averaged velocity of the droplet. (b) Upper panel: average shear rate at the contact surface,  $\dot{\gamma}_{cs}$ ; Lower panel: droplet contact surface area. Square markers represent the substrate velocities, while dot markers indicate the measured quantities. Pairs of square and dot markers with the same color correspond to the same time intervals in Figure 8.

Substrate velocity,  $u_{sub}$ , is represented by dashed lines.

asymmetric shape (Figure 8(a) and (c)). We also observe in the case of Phase I droplets, that the periodic oscillations attain a steady periodic motion after a few oscillations. This shift to a steady motion is best seen in this example in the contact surface area  $A_{cs}$  (Figure 9(b)). The area requires a larger time scale than the other observables to reflect a steady state. In this particular example, this time is about four complete oscillations, and a somewhat periodic pattern then appears in the data regarding the contact area with a shorter and a longer time scale. Similar patterns have been observed for Phase I oscillations regardless of droplet size and substrate wettability (see e.g. width and area in Figure 7, where the steady oscillation is attained faster), suggesting it is a general feature.

## 2. Phase II oscillation

When the substrate becomes more wettable, instabilities find it easier to arise, leading to the eventual breakup of the droplet for a certain range of substrate vibration amplitude and frequency (see Figure 5 for the exact values for different contact-angle cases). We will refer to the scenario in

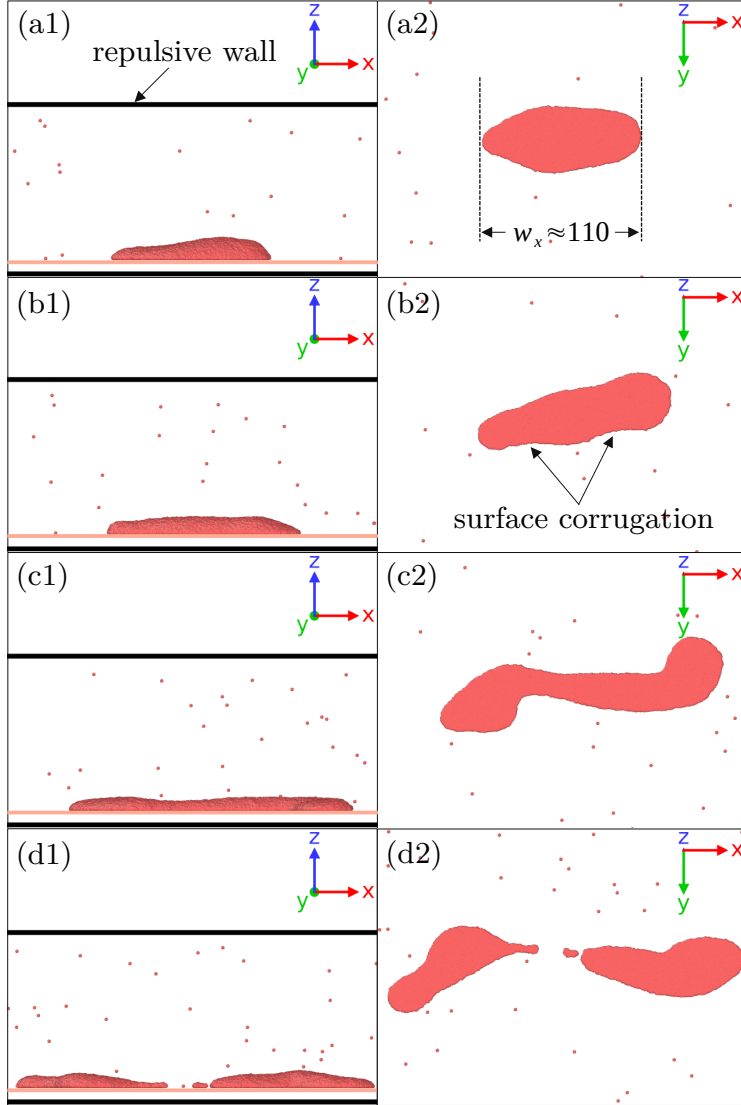


FIG. 10: Example of Phase II oscillation, with time progressing from (a) to (d).  $N = 20 \times 10^4$ ,  $\epsilon_{ws} = 3.0$  ( $\theta = 50^\circ$ ),  $A_{\text{sub}} = 450$ ,  $f_{\text{sub}} = 7.5 \times 10^{-3}$ . The simulation box boundary is indicated. (a1) Side view; (a2) bottom view at the contact surface, at the same moment as (a1), showing the droplet in a symmetric shape. (b1, b2) Internal rotation and stretching develops. (c1, c2) The droplet stretches further and deviates significantly from a spherical-cap shape. (d1, d2) Droplet break-up occurs. Panels correspond to times  $t = 837, 1532, 2837, 3020$  in Figure 11.

which this occurs after some build-up as Phase II oscillation. A typical Phase II droplet oscillation is presented in Figure 10. In particular, the droplet initially exhibits oscillations as in Phase I. However, larger conformation changes are recorded during the simulation and stretching ensues with a rate that is not tied to the oscillation frequency. An internal rotation then develops within

the droplet, resulting in the surface corrugation that rotates along the contact line, as shown in panel (b) of Figure 10. This phenomenon will be discussed in detail later. Consequently, the droplet assumes an asymmetric shape (in the sense that the droplet considerably deviates from a spherical-cap shape), as depicted in panel (c) of Figure 10. As a result, the left and right domains of the droplet rotate with a certain momentum, causing these domains to move apart and eventually leading to the break-up of the droplet as shown in panel (d) of Figure 10. Moreover, the formation of satellite droplets is observed through a mechanism that has been described in a previous study.<sup>6</sup>

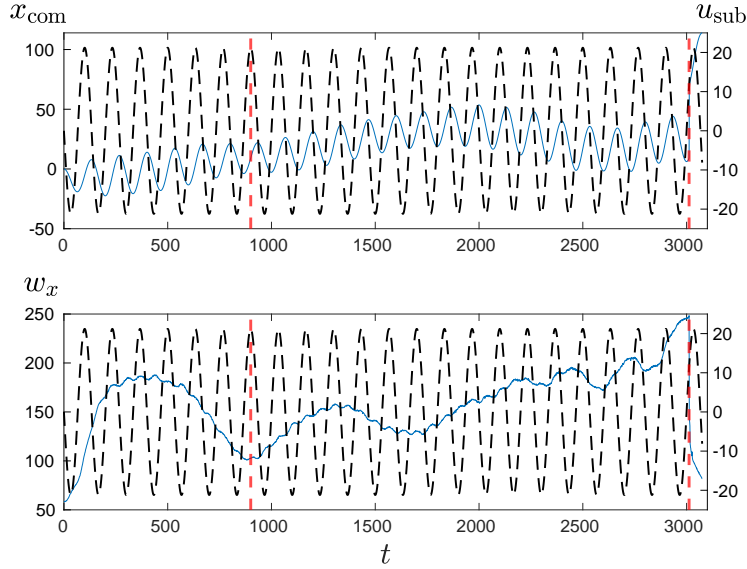


FIG. 11: Phase II oscillation of the same droplet as in Figure 10. (Upper panel)  $x_{\text{com}}$ : center of mass of the droplet; (Lower panel)  $w_x$ : width of the droplet in the  $x$  direction at the contact surface, in comparison with the substrate velocity,  $u_{\text{sub}}$  (indicated by the dashed line in each graph). The asymmetric shape of the droplet, begins to appear around  $t \sim 900$  and develops to the rotated asymmetric shape as shown in Figure 10(b). Droplet breakup occurs at  $t = 3012$ , after which the separated droplets oscillate apart as shown in Figure 10(d). Only the larger droplet is tracked after the breakup. Both events are marked by red dashed vertical lines. Plots are obtained from a single trajectory.

To gain further insights into the mechanisms of Phase II oscillations, as in the case of Phase I, we have carefully examined various parameters of the droplets and made comparison with the Phase I oscillation. Figure 11 presents the center-of-mass oscillations of the droplet in the  $x$  direction,  $x_{\text{com}}$ , and the droplet width in the direction along the oscillation at the contact surface,  $w_x$  (see Figure 10(a) for the definition of the droplet width), up to the point of droplet breakup.

They are compared to the substrate velocity,  $u_{\text{sub}}$ . In Phase II,  $x_{\text{com}}$  appears to have a phase shift of one-quarter relative to  $u_{\text{sub}}$  during the repeated vibration cycles, as also seen in Phase I. However, a more significant drift in the position  $x_{\text{com}}$  of the droplet is observed in comparison with Phase I. This difference in behavior between  $x_{\text{com}}$  and  $u_{\text{sub}}$  persists over the entire oscillation period. Two key distinctions between Phase I and Phase II oscillations are the emergence of significant out-of-phase stretching and the development of asymmetric internal rotation within the droplet (shown in later figures). Phase II oscillations are observed to occur under moderate oscillation amplitudes and frequencies (Figure 5), where the droplet becomes elongated without immediate breakup. While in Phase I the droplet width,  $w_x$ , closely follows the oscillation pattern of the substrate, in Phase II,  $w_x$  follows a much longer period than the substrate vibrations. This pattern maintains until the droplet becomes highly asymmetric, at which point a non-monotonic change in  $w_x$  occurs (around  $t \sim 1700$  in Figure 11), ultimately leading to the droplet breakup. Moreover, the elongation of  $w_x$  is significantly greater in Phase II. For instance, in the Phase I example (Figure 7), the maximum elongation is approximately  $\sim 40\%$  longer than the static droplet's width, whereas in Phase II (Figure 11), the maximum elongation reaches about  $\sim 200\%$ . This extreme elongation decouples different sections of the droplet, making them susceptible to independent fluctuations that intensify over time and amplify the droplet's asymmetry, as shown in panel (b) and (c) of Figure 10. The oscillating droplet eventually becomes highly asymmetric, resulting in breakups as shown in panel (d) of Figure 10. The increasing asymmetry in the shape of the droplet is evident from the non-monotonic behavior of  $w_x$ , and the contact surface area  $A_{\text{CS}}$ , over time.

To explore closer the velocities of the droplet particles at the liquid–solid interface, here, we revisit Phase II oscillation with parameters identical to those in Figure 10 and 11, but with a different initial velocity seed and a shorter simulation duration before breakup, as illustrated in Figure 12 and 13. Initially, the velocity field within the elongated droplet aligns with the substrate's motion (Figure 12(a)). The droplet then starts to exhibit a rotational velocity field that provides angular momentum to the droplet (Figure 12(b)). This results in a rotational motion of the droplet, reflected in the rotation of the surface corrugation, increasing its asymmetry (Figure 12(c)) and ultimately culminating in the breakup of the droplet. The timing of the development of the asymmetric velocity field, shape and the droplet breakup is stochastic. In the two cases illustrated in Figure 10 and Figure 12, the same oscillation parameters with different initial velocity seeds yield distinct asymmetric droplet shapes and different breakup times. However, the oscillation of the droplet width in Figure 11 and the contact area in Figure 13 follows the same long-time oscillation. Moreover, the

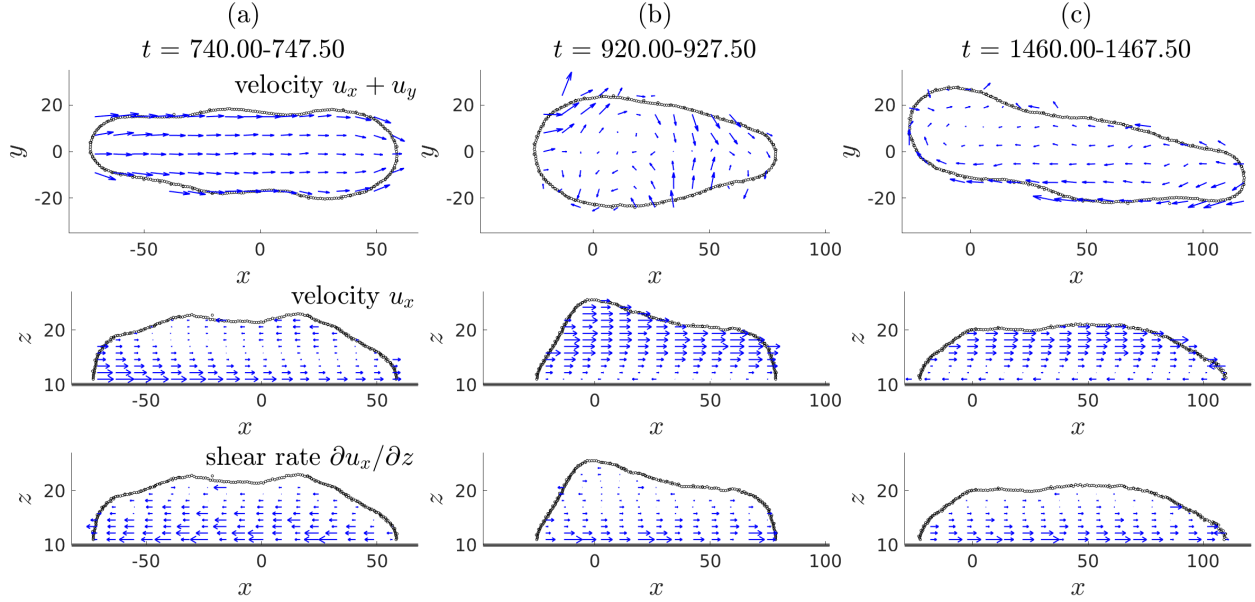


FIG. 12: Phase II oscillation with identical parameters to Figure 10, using a different velocity seed. Upper panels: time-averaged velocity field at (a)  $t = 740 \sim 747.5$  when the droplet exhibits a elongated shape, (b)  $t = 920 \sim 927.5$  when velocity-field and rotation begins to develop, (c)  $t = 1460 \sim 1467.5$  when the droplet's velocity field is highly asymmetric. Middle panels: time-averaged velocity field in the  $x$  direction at the cross-section  $y = 0$ , taken over the same time intervals as the top row. Lower panels: time-averaged shear rate at each stage. Each velocity field is time-averaged from four sequential frames.

velocity profiles in Figure 12 and the corresponding shear rates at the particular times shown here, indicate that there is a significant difference in the magnitude of the velocity between the particles located at the bottom of the droplet and those closer to the apex. This clearly shows that the upper particles cannot fully synchronize with the vibration induced by the substrate. Consequently, we reason that a sufficiently large thermal random fluctuation, particularly near the apex, can result in the asymmetry of the velocity field observed in Figure 12, leading to the droplet's rotational motion.

From both Phase II simulations, we observe that the center-of-mass of the droplet,  $x_{\text{com}}$ , follows the periodicity of the substrate and droplet velocity, but with a phase lag of one-quarter of the oscillation period (Figure 11 and 13(a)). However, this alignment only persists until the time that the breakup occurs (Figure 11). Prior to the breakup,  $x_{\text{com}}$ ,  $\bar{u}_x$  and  $\dot{\gamma}_{\text{cs}}$  exhibit periodic patterns (Figure 13) similar to those in Phase I oscillation. The oscillation of  $w_x$  in Figure 11 and  $A_{\text{cs}}$  in

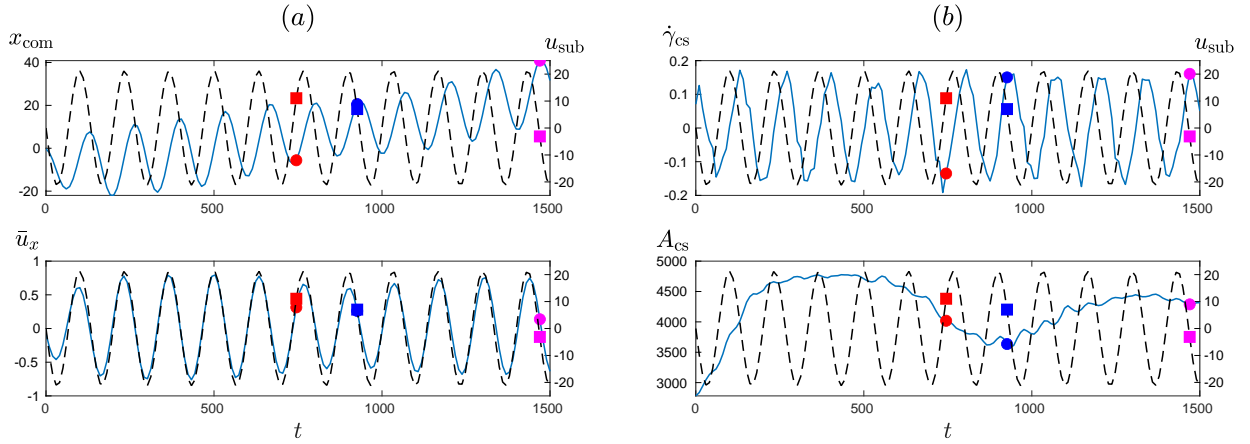


FIG. 13: (a) Upper panel: center-of-mass position of the droplet from Figure 12, with a different seed to Figure 11; Lower panel: averaged droplet velocity. (b) Upper panel: average shear rate at the contact surface,  $\dot{\gamma}_{cs}$ ; Lower panel: droplet contact surface area. Square markers represent substrate velocities, while dot markers indicate measured quantities. Pairs of square and dot markers with the same color correspond to matching time intervals in Figure 12. Substrate velocity  $u_{sub}$  is represented by dashed lines.

Figure 13 follows the same long-time oscillation with significant amplitudes. These observations suggest that the substrate vibrations introduce a systematic driving of the droplet width, progressively increasing asymmetry, and ultimately leading to oscillations that cause the droplet to split apart.

### 3. Phase III Oscillation

A typical scenario of Phase III oscillation behavior is demonstrated in Figure 14. In the example presented here, the droplet is subjected to the same oscillation frequency,  $f_{sub} = 7.5 \times 10^{-3}$ , as in the previous Phase II example. However, by increasing the oscillation amplitude to  $A_{sub} = 675$ , the droplet transitions to Phase III oscillation. In this phase, the droplet rapidly elongates due to a high shear rate that eventually leads to the droplet breakup.

In Phase III, the center-of-mass of the droplet,  $x_{com}$ , follows the periodic motion of the substrate vibration, but with a continuous drifting that gradually increases (Figure 15). This drifting might be due to the continuous elongation of the droplet, which is indicated by monitoring its width,

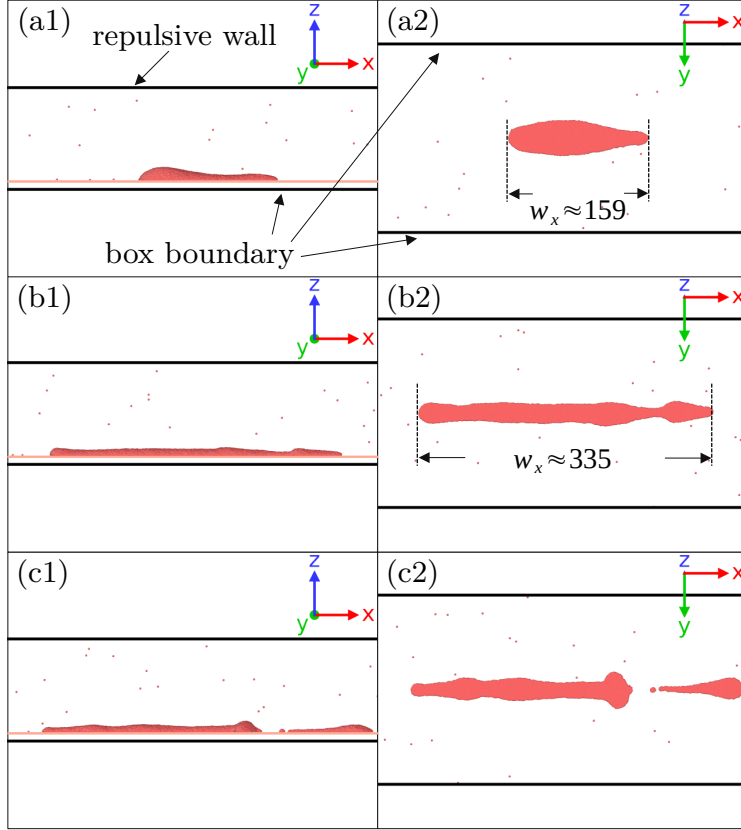


FIG. 14: Example of phase III oscillation with parameters:  $N = 20 \times 10^4$ ,  $\epsilon_{ws} = 3.0$  ( $\theta = 50^\circ$ ),  $A_{\text{sub}} = 675$ ,  $f_{\text{sub}} = 7.5 \times 10^{-3}$ . (a1) side view; (a2) bottom view at the contact surface, taken at the same moment as (a1), showing the elongated configuration of the droplet. (b1,2) droplet is highly elongated. (c1,2) droplet undergoes break-up. Panels correspond to times  $t = 100, 350, 450$  in Figure 15.

$w_x$ . The width steadily increases until the breakup of the droplet, in contrast to the variable and non-monotonic change observed in the breakup of Phase II oscillations. After the breakup, only the larger droplet is tracked. The sudden shift in  $x_{\text{com}}$  that is seen when the breakup occurs comes from omission of the smaller droplet from the cluster used to calculate quantities.

By monitoring the velocity profile (Figure 16), we observe that the two domains of the droplet can move in opposite directions during the elongation stage (middle panel of Figure 16(a)). This opposing motion results in the extreme elongation of the droplet during the initial oscillations. At the time of the breakup, it is clearly seen that the velocity in the region where the two droplets begin to separate differs from the velocity at the centers of the two forming droplets (middle panel of Figure 16(b)). Similar to Phase II, random thermal fluctuations alter the breakup time.

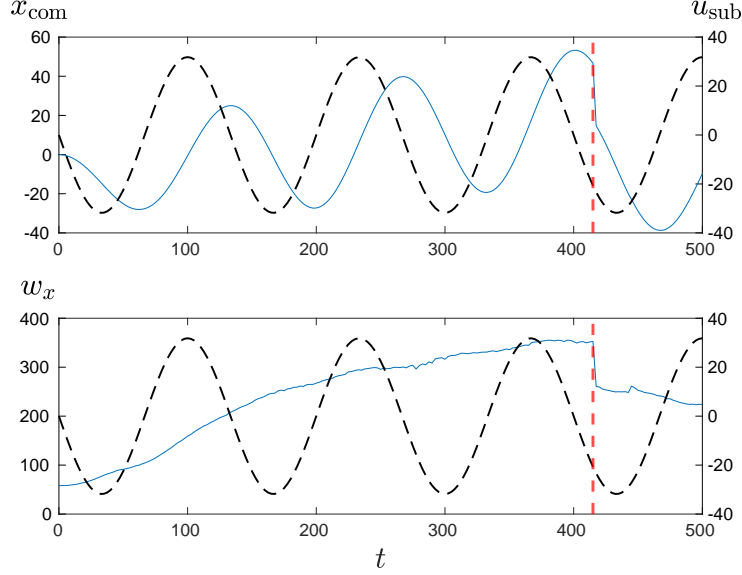


FIG. 15: Phase III oscillation of the same droplet as shown in Figure 14. (Upper panel)  $x_{\text{com}}$ : center of mass of the droplet; (Lower panel)  $w_x$ : width of the droplet in the  $x$  direction at the contact surface, compared with the substrate velocity (dashed lines),  $u_{\text{sub}}$ . The red vertical dashed line at  $t = 412$  marks the point at which the droplet undergoes breakup. Only the larger droplet is tracked after the breakup.

In the two examples shown in Figures 14 and 15, and Figures 16 and 17, both examples have the same oscillation parameters but different initial velocity seeds, resulting in different breakup times. However, in contrast to the rotation motion observed in the case of Phase II, the breakup in Phase III does not require such rotational dynamics. This can be better explained by examining the shear profiles in the lower panel of Figure 16(b), where we can see that two significant shear regions have developed within the droplet, located near the centers of the two forming droplets. In contrast, the shear in the region between the two forming droplets is significantly lower. This difference in shear eventually leads to the breakup.

### C. Phase transition and droplet dynamics at the contact surface

In the previous sections, we have examined the role of droplet elongation in each phase of droplet oscillation. In the state diagram shown in Figure 5, it is evident that for the same substrate amplitude,  $A_{\text{sub}}$ , and frequency,  $f_{\text{sub}}$  (and thus the same velocity amplitude  $u_{\text{sub}}$ ), increasing wettability induces a phase transition from a lower phase to a higher one. The increase in wettability

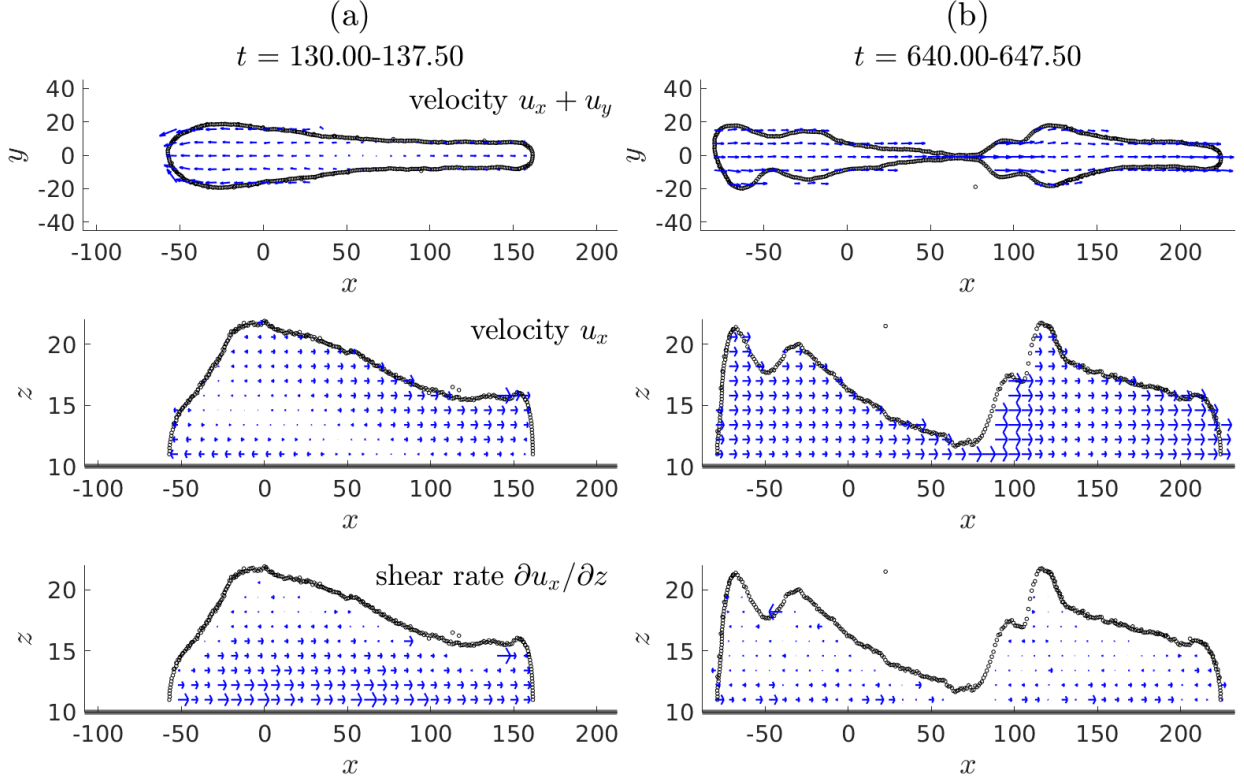


FIG. 16: Phase III oscillation with identical parameters to Figure 14, using a different velocity seed. Upper panels: time-averaged velocity field at (a)  $t = 130 \sim 137.5$  when the droplet is elongated in shape, and (b)  $t = 640 \sim 647.5$  at the moment before the droplet breakup. Middle panels: time-averaged velocity field in the  $x$  direction at the cross-section, over the same time intervals as the top row. Lower panels: time-averaged shear rate. Each velocity field is time-averaged from four sequential frames.

enhances the interaction between the droplet particles and the substrate surface, resulting in higher particle velocities, particularly at the contact surface. Figure 18 illustrates the magnitude of the average particle velocity in the  $x$  direction at the contact surface,  $|\bar{u}_{x,cs}|$ , and its corresponding phase as observed in the simulation.

Figure 18 corresponds to the state diagram for the particle number  $N = 20 \times 10^4$  in Figure 5. This figure clearly demonstrates that the magnitude of the average particle velocity at the contact surface,  $|\bar{u}_{x,cs}|$ , aligns with the oscillation phase of the droplet. In general, across all equilibrium contact angles,  $\theta$ , the droplet exhibits Phase I oscillation when  $|\bar{u}_{x,cs}| \ll 1$ . There is a monotonic dependence of phase on  $|\bar{u}_{x,cs}|$ , with low values corresponding to Phase I, high  $|\bar{u}_{x,cs}| \gg 1$  to phase III, and under sufficient wetting  $\theta \lesssim 90^\circ$ , Phase II appears in the vicinity of  $|\bar{u}_{x,cs}| \sim 1$ .

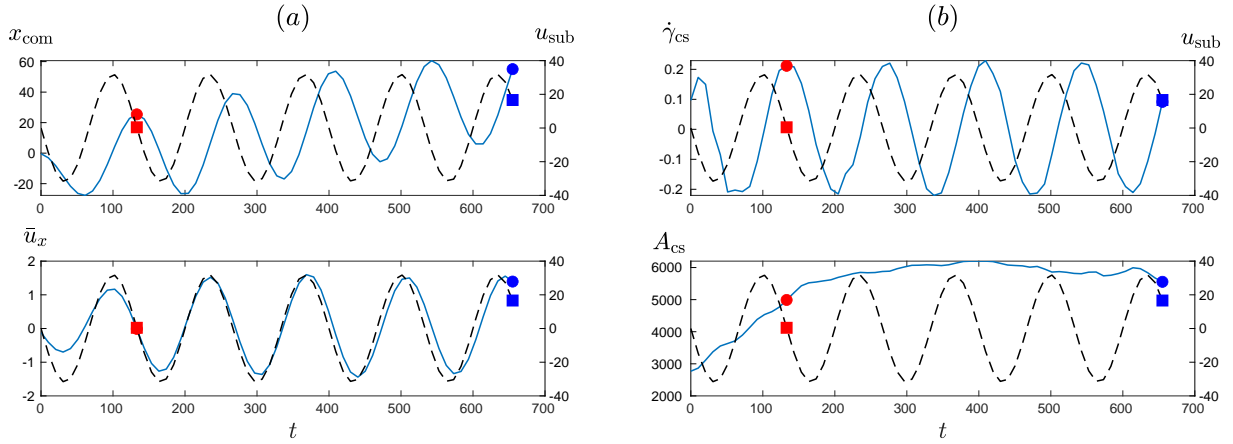


FIG. 17: (a) Upper panel: center-of-mass position of the droplet described in Figure 16; Lower panel: averaged droplet velocity. (b) Upper panel: average shear rate at the contact surface,  $\dot{\gamma}_{cs}$ ; Lower panel: droplet contact surface area. Square markers represent substrate velocities, while dot markers indicate measured quantities. Pairs of square and dot markers with the same color correspond to matching time intervals in Figure 16. The blue markers at  $t = 640 \sim 647.5$  correspond to the moment before the droplet breakup. Substrate velocity  $u_{sub}$  is represented by dashed lines.

These results, as shown in Figure 18, suggest that the contact surface velocity of the droplet, and consequently the capillary number, plays a critical role in determining the three phases observed in droplet oscillation.

#### IV. CONCLUSIONS

In this study, we have taken steps to investigate the oscillations of water droplets on horizontally, harmonically, vibrating substrates. The simulation approach followed here offers specific advantages with regards to experiments and continuum simulation, such as the flawless control over various conditions and parameters during the simulation experiment and the natural ability of particle-based simulation to conduct the analysis with a molecular resolution. The main findings of this study are as follows:

1. **Oscillation Phases:** Droplet oscillations are categorized into three phases based on substrate vibration amplitude and frequency:

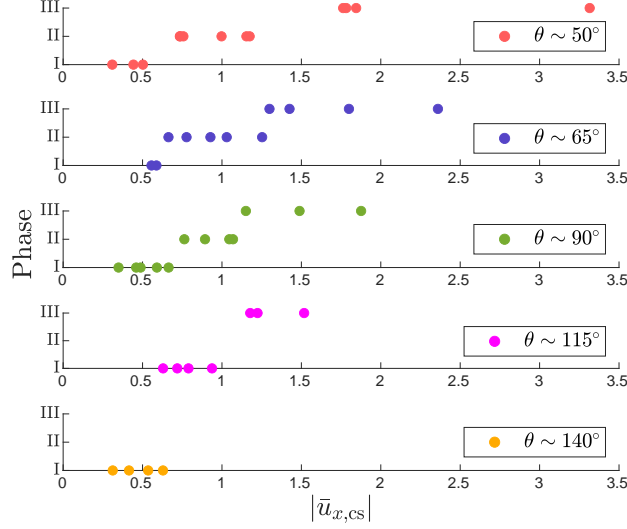


FIG. 18: Phase versus the magnitude of the average  $x$ -velocity of the particles at the contact surface,  $|\bar{u}_{x,cs}|$ , for droplets with various equilibrium contact angles  $\theta$ . Number of particles  $N = 20 \times 10^4$ .

- **Phase I:** Present for both hydrophobic and hydrophilic substrates.
- **Phases II & III:** More common in hydrophilic substrates, specifically at higher frequencies and amplitudes.

We obtained the state diagrams for various droplet sizes.

2. **Droplet Dynamics and Shear Stress:** The droplet properties and oscillatory behavior were analyzed with respect to the periodic motion of the substrate. We highlighted the critical role of internal shear stress in droplet breakup.
3. **Phase I Dynamics:** Variations in contact angles relative to the substrate velocity in Phase I oscillations at different oscillation amplitudes, frequencies, and droplet–substrate affinities were observed. Future work will explore the contact angle differences and related dynamics in greater detail.
4. **Capillary Number Influence:** The magnitude of the average particle velocity at the contact surface plays a key role in determining the three oscillation phases, suggesting that the phase behavior is governed by the capillary number of the oscillating droplet.

In summary, this study provides insights into the dynamics of droplet oscillations on harmonically vibrating substrates, hitherto inaccessible to continuum simulation and experiment.

## V. SUPPLEMENTARY MATERIAL

These are the state diagrams for medium ( $N = 10 \times 10^4$ ) and smaller ( $N = 5 \times 10^4$ ) sized droplets.

## ACKNOWLEDGMENTS

This research has been supported by the National Science Centre, Poland, under grant No. 2019/34/E/ST3/00232. We gratefully acknowledge Polish high-performance computing infrastructure PLGrid (HPC Center: ACK Cyfronet AGH) for providing computer facilities and support within computational grant no. PLG/2023/016608. TB and MK acknowledge support from Warsaw University of Technology within the Excellence Initiative: Research University (IDUB) programme.

## REFERENCES

- <sup>1</sup>D. S. Dkhar, R. Kumari, S. J. Malode, N. P. Shetti, and P. Chandra, “Integrated lab-on-a-chip devices: Fabrication methodologies, transduction system for sensing purposes,” *J. Pharm. Biomed. Anal.* **223**, 115120 (2023).
- <sup>2</sup>S. D. Hoath, *Fundamentals of Inkjet Printing: The Science of Inkjet and Droplets* (John Wiley & Sons, Cambridge, 2016).
- <sup>3</sup>J. Yin, S. Wang, X. Sang, Z. Zhou, B. Chen, P. Thrassos, A. Romeos, and A. Giannadakis, “Spray cooling as a high-efficient thermal management solution: A review,” *Energies* **15**, 8547 (2022).
- <sup>4</sup>O. R. Kummitha, “The impact of wedge and wavy-wall combustor side walls on shock-induced mixing and combustion in a hydrogen-fuelled model scramjet combustor,” *Int. J. Hydrog. Energy* **74**, 161–169 (2024).
- <sup>5</sup>J. V. Timonen, M. Latikka, O. Ikkala, and R. H. Ras, “Free-decay and resonant methods for investigating the fundamental limit of superhydrophobicity,” *Nat. Commun.* **4** (2013), 10.1038/ncomms3398.
- <sup>6</sup>L. H. Carnevale, P. Deuar, Z. Che, and P. E. Theodorakis, “Liquid thread breakup and the formation of satellite droplets,” *Phys. Fluids* **35**, 074108 (2023).

- <sup>7</sup>F. Mugele, J.-C. Baret, and D. Steinhauser, “Microfluidic mixing through electrowetting-induced droplet oscillations,” *Appl. Phys. Lett.* **88** (2006), 10.1063/1.2204831.
- <sup>8</sup>S. Daniel, M. K. Chaudhury, and P. G. D. Gennes, “Vibration-actuated drop motion on surfaces for batch microfluidic processes,” *Langmuir* **21**, 4240–4248 (2005).
- <sup>9</sup>M. Junaid, H. A. Nurmi, M. Latikka, M. Vuckovac, and R. H. Ras, “Oscillating droplet tribometer for sensitive and reliable wetting characterization of superhydrophobic surfaces,” *Droplet* **1**, 38–47 (2022).
- <sup>10</sup>H. Rodot, C. Bisch, and A. Lasek, “Zero-gravity simulation of liquids in contact with a solid surface,” *Acta Astronaut.* **6**, 1083–1092 (1979).
- <sup>11</sup>A. J. Milne, B. Defez, M. Cabrerizo-Vílchez, and A. Amirfazli, “Understanding (sessile/constrained) bubble and drop oscillations,” *Adv. Colloid Interface Sci.* **203**, 22–36 (2014).
- <sup>12</sup>J. Rayleigh, *Axisymmetric oscillations of free spherical drop. The theory of sound, vol2* (Dover, 1945).
- <sup>13</sup>S. Chandrasekhar, *Hydrodynamic and Hydromagnetic Stability* (Oxford University Press, 1961).
- <sup>14</sup>S. Mettu and M. Chaudhury, “Motion of drops on a surface induced by thermal gradient and vibration,” *Langmuir* **24**, 10833–10837 (2008).
- <sup>15</sup>D. V. Lyubimov, T. P. Lyubimova, and S. V. Shklyayev, “Behavior of a drop on an oscillating solid plate,” *Phys. Fluids* **18** (2006), 10.1063/1.2137358.
- <sup>16</sup>L. Kelvin, *In: Mathematical and Physical Papers, Vol. III* (C.J. Clay and Sons, 1890).
- <sup>17</sup>H. Lamb, “On the oscillations of a viscous spheroid,” *Proc. London Math. Soc.* **s1-13**, 51–70 (1881).
- <sup>18</sup>E. Pierce, F. J. Carmona, and A. Amirfazli, “Understanding of sliding and contact angle results in tilted plate experiments,” *Colloids Surf. A: Physicochem. Eng. Asp.* **323**, 73–82 (2008).
- <sup>19</sup>P. Brunet, J. Eggers, and R. D. Deegan, “Vibration-induced climbing of drops,” *Phys. Rev. Lett.* **99** (2007), 10.1103/PhysRevLett.99.144501.
- <sup>20</sup>R. A. Huber, M. Campbell, N. Doughramaji, and M. M. Derby, “Vibration-enhanced droplet motion modes: Simulations of rocking, ratcheting, ratcheting with breakup, and ejection,” *J. Fluids Eng.* **141** (2019), 10.1115/1.4042037.
- <sup>21</sup>E. S. Benilov and J. Billingham, “Drops climbing uphill on an oscillating substrate,” *J. Fluid Mech.* **674**, 93–119 (2011).
- <sup>22</sup>E. Becker, W. J. Hiller, and T. A. Kowalewski, “Experimental and theoretical investigation of large-amplitude oscillations of liquid droplets,” *J. Fluid Mech.* **231**, 189–210 (1991).

- <sup>23</sup>E. Becker, W. J. Hiller, and T. A. Kowalewski, “Nonlinear dynamics of viscous droplets,” *J. Fluid Mech.* **258**, 191–216 (1994).
- <sup>24</sup>A. Rahimzadeh, T. Khan, and M. Eslamian, “Experiments and modeling of nonlinear frequency response of oscillations of a sessile droplet subjected to horizontal vibrations,” *Eur. Phys. J. E* **42**, 125 (2019).
- <sup>25</sup>M. A. Pyankova and A. A. Alabuzhev, “Influence of the properties of the plate surface on the oscillations of the cramped drop,” *Phys. Fluids* **34** (2022), 10.1063/5.0101011.
- <sup>26</sup>L. Dong, A. Chaudhury, and M. K. Chaudhury, “Lateral vibration of a water drop and its motion on a vibrating surface,” *Eur. Phys. J. E* **21**, 231–242 (2006).
- <sup>27</sup>F. Celestini and R. Kofman, “Vibration of submillimeter-size supported droplets,” *Phys. Rev. E* **73** (2006), 10.1103/PhysRevE.73.041602.
- <sup>28</sup>H. Ding, M. N. Gilani, and P. D. Spelt, “Sliding, pinch-off and detachment of a droplet on a wall in shear flow,” *J. Fluid Mech.* **644**, 217–244 (2010).
- <sup>29</sup>T. D. Blake, “The physics of moving wetting lines,” *J. Colloid. Interface Sci.* **299**, 1–13 (2006).
- <sup>30</sup>S. Daniel and M. K. Chaudhury, “Rectified motion of liquid drops on gradient surfaces induced by vibration,” *Langmuir* **18**, 3404–3407 (2002).
- <sup>31</sup>T. Zhang, P. Zhou, T. Simon, and T. Cui, “Internal flow in sessile droplets induced by substrate oscillation: towards enhanced mixing and mass transfer in microfluidic systems,” *Microsyst. Nanoeng.* **10** (2024), 10.1038/s41378-024-00714-4.
- <sup>32</sup>P. Deepu, S. Chowdhuri, and S. Basu, “Oscillation dynamics of sessile droplets subjected to substrate vibration,” *Chem. Eng. Sci.* **118**, 9–19 (2014).
- <sup>33</sup>P. Gilewicz, *Dynamic measurement of the contact angle hysteresis*, Master’s thesis, Warsaw University of Technology (2023).
- <sup>34</sup>J. S. Sharp, D. J. Farmer, and J. Kelly, “Contact angle dependence of the resonant frequency of sessile water droplets,” *Langmuir* **27**, 9367–9371 (2011).
- <sup>35</sup>J. S. Sharp, “Resonant properties of sessile droplets; contact angle dependence of the resonant frequency and width in glycerol/water mixtures,” *Soft Matter* **8**, 399–407 (2012).
- <sup>36</sup>M. Strani and F. Sabetta, “Free vibrations of a drop in partial contact with a solid support,” *J. Fluid Mech.* **141**, 233–247 (1984).
- <sup>37</sup>M. Chiba, S. Michiue, and I. Katayama, “Free vibration of a spherical liquid drop attached to a conical base in zero gravity,” *J. Sound Vib.* **331**, 1908–1925 (2012).

- <sup>38</sup>Noblin, X., Buguin, A., and Brochard-Wyart, F., “Vibrated sessile drops: Transition between pinned and mobile contact line oscillations,” *Eur. Phys. J. E* **14**, 395–404 (2004).
- <sup>39</sup>T. Kalmar-Nagy and B. Balachandran, *The Duffing Equation: Nonlinear Oscillators and their Behaviour*, edited by I. Kovacic and M. J. Brennan (John Wiley & Sons, 2011).
- <sup>40</sup>L. Chen, E. Bonaccorso, P. Deng, and H. Zhang, “Droplet impact on soft viscoelastic surfaces,” *Phys. Rev. E* **94**, 063117 (2016).
- <sup>41</sup>S. Lin, B. Zhao, S. Zou, J. Guo, Z. Wei, and L. Chen, “Impact of viscous droplets on different wettable surfaces: Impact phenomena, the maximum spreading factor, spreading time and post-impact oscillation,” *J. Colloid Interface Sci.* **516**, 86–97 (2018).
- <sup>42</sup>M.-s. Li, J. Wen, H.-b. Hu, L. Xie, and L.-z. Ren, “Scaling laws of droplets on vibrating liquid-infused surfaces,” *Phys. Fluids* **36**, 082112 (2024).
- <sup>43</sup>D. C. Rapaport, *The Art of Molecular Dynamics Simulation*, 2nd ed. (Cambridge University Press, 2004).
- <sup>44</sup>P. E. Theodorakis, E. A. Müller, R. V. Craster, and O. K. Matar, “Superspreading: Mechanisms and molecular design,” *Langmuir* **31**, 2304–2309 (2015).
- <sup>45</sup>L. H. Carnevale, P. Deuar, Z. Che, and P. E. Theodorakis, “Surfactant-laden liquid thread breakup driven by thermal fluctuations,” *Phys. Fluids* **36**, 033301 (2024).
- <sup>46</sup>L. H. Carnevale and P. E. Theodorakis, “Many-body dissipative particle dynamics with the martini lego approach,” *Eur. Phys. J. Plus* **139**, 539 (2024).
- <sup>47</sup>P. J. Hoogerbrugge and J. M. V. A. Koelman, “Simulating Microscopic Hydrodynamic Phenomena with Dissipative Particle Dynamics,” *Europhys. Lett. (EPL)* **19**, 155–160 (1992).
- <sup>48</sup>E. Lavagnini, J. L. Cook, P. B. Warren, and C. A. Hunter, “Translation of chemical structure into dissipative particle dynamics parameters for simulation of surfactant self-assembly,” *J. Phys. Chem. B* **125**, 3942–3952 (2021).
- <sup>49</sup>I. Pagonabarraga and D. Frenkel, “Non-Ideal DPD Fluids,” *Mol. Simul.* **25**, 167–175 (2000).
- <sup>50</sup>P. B. Warren, “Vapor-liquid coexistence in many-body dissipative particle dynamics,” *Phys. Rev. E* **68**, 066702 (2003).
- <sup>51</sup>R. D. Groot and P. B. Warren, “Dissipative particle dynamics: Bridging the gap between atomistic and mesoscopic simulation,” *J. Chem. Phys.* **107**, 4423–4435 (1997).
- <sup>52</sup>A. P. Thompson, H. M. Aktulga, R. Berger, D. S. Bolintineanu, W. M. Brown, P. S. Crozier, P. J. in ’t Veld, A. Kohlmeyer, S. G. Moore, T. D. Nguyen, R. Shan, M. J. Stevens, J. Tranchida,

- C. Trott, and S. J. Plimpton, “LAMMPS - a flexible simulation tool for particle-based materials modeling at the atomic, meso, and continuum scales,” *Comp. Phys. Comm.* **271**, 108171 (2022).
- <sup>53</sup>P. B. Warren, “No-go theorem in many-body dissipative particle dynamics,” *Phys. Rev. E* **87**, 045303 (2013).
- <sup>54</sup>P. Vanya, P. Crout, J. Sharman, and J. A. Elliott, “Liquid-phase parametrization and solidification in many-body dissipative particle dynamics,” *Phys. Rev. E* **98**, 033310 (2018).
- <sup>55</sup>P. Español and P. Warren, “Statistical Mechanics of Dissipative Particle Dynamics,” *Europhys. Lett. (EPL)* **30**, 191–196 (1995).
- <sup>56</sup>P. Zhou, J. Hou, Y. Yan, J. Wang, and W. Chen, “Effect of Aggregation and Adsorption Behavior on the Flow Resistance of Surfactant Fluid on Smooth and Rough Surfaces: A Many-Body Dissipative Particle Dynamics Study,” *Langmuir* **35**, 8110–8120 (2019).
- <sup>57</sup>A. Ghoufi and P. Malfreyt, “Mesoscale modeling of the water liquid-vapor interface: A surface tension calculation,” *Phys. Rev. E* **83**, 051601 (2011).
- <sup>58</sup>M. Arienti, W. Pan, X. Li, and G. Karniadakis, “Many-body dissipative particle dynamics simulation of liquid/vapor and liquid/solid interactions,” *J. Chem. Phys.* **134**, 204114 (2011).
- <sup>59</sup>P. E. Theodorakis, E. A. Müller, R. V. Craster, and O. K. Matar, “Modelling the superspreading of surfactant-laden droplets with computer simulation,” *Soft Matter* **11**, 9254–9261 (2015).
- <sup>60</sup>P. E. Theodorakis, Y. Wang, A. Chen, and B. Liu, “Off-lattice monte-carlo approach for studying nucleation and evaporation phenomena at the molecular scale,” *Materials* **14** (2021), 10.3390/ma14092092.
- <sup>61</sup>A. Stukowski, “Visualization and analysis of atomistic simulation data with ovito—the open visualization tool,” *Modelling Simul. Mater. Sci. Eng.* **18**, 015012 (2010).
- <sup>62</sup>P. E. Theodorakis, W. Paul, and K. Binder, “Analysis of the cluster formation in two-component cylindrical bottle-brush polymers under poor solvent conditions. a simulation study,” *Eur. Phys. J. E* **34**, 52 (2011).

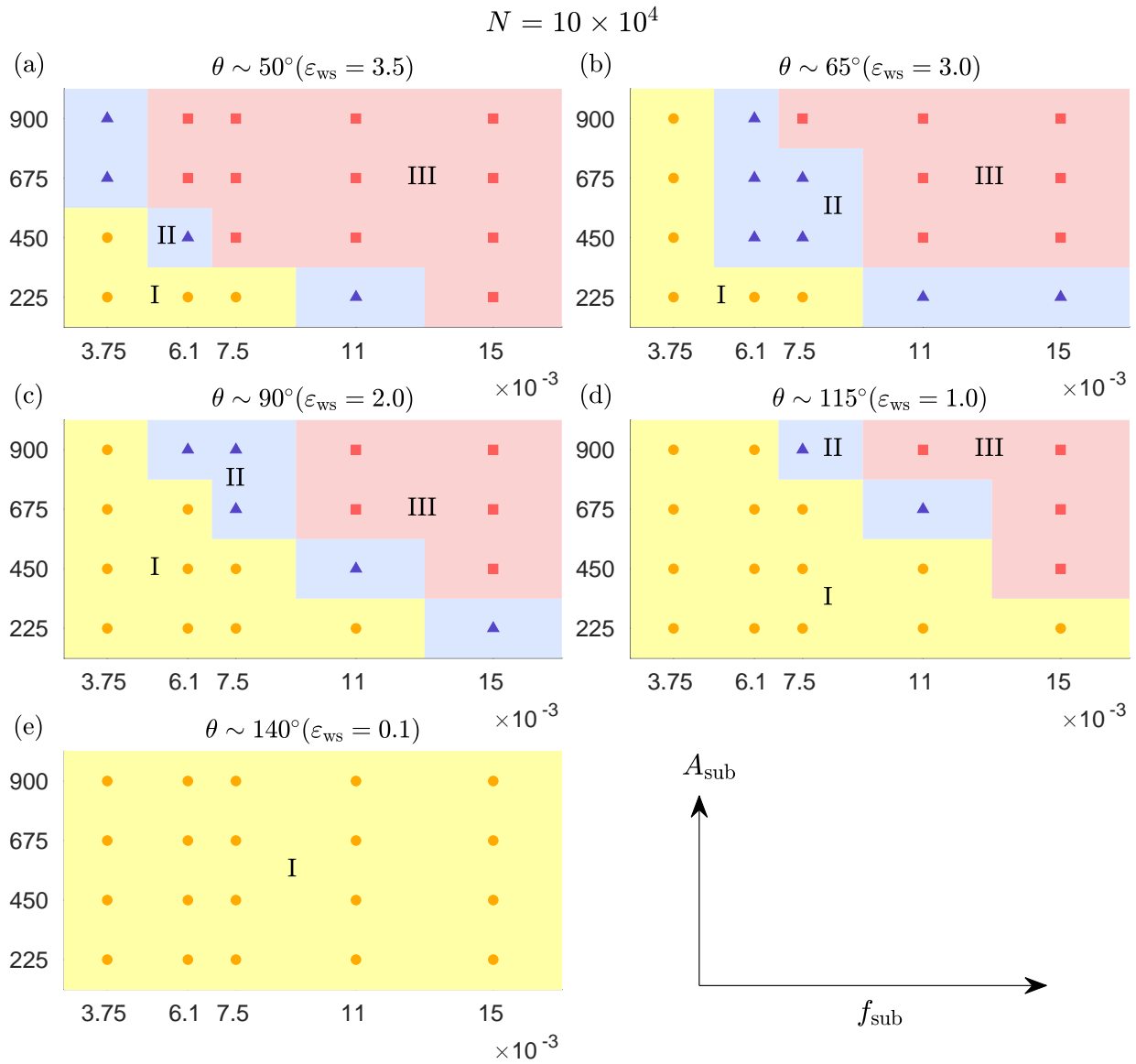


FIG. 19: State diagram for droplet with number of particles  $N = 10 \times 10^4$  at each initial static contact angle  $\theta$ .

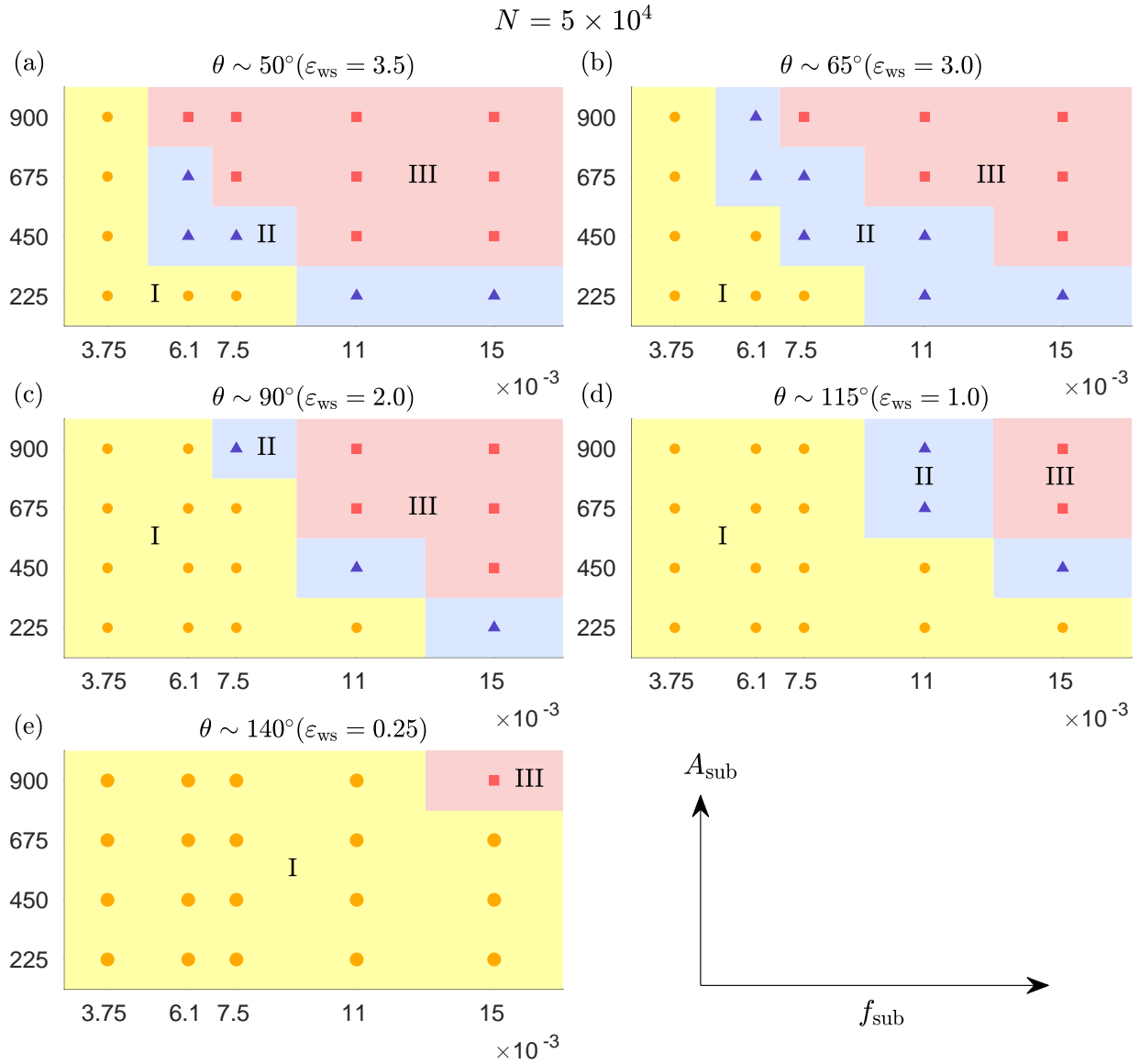


FIG. 20: State diagram for droplet with number of particles  $N = 5 \times 10^4$  at each initial static contact angle  $\theta$ .